ChemComm

REVIEW ARTICLE

View Article Online
View Journal | View Issue

Cite this: *Chem. Commun.*, 2026, **62**, 11802

Mapping reaction pathways and catalyst dynamics in electrochemical CO_2 reduction through *in situ* and *operando* characterisation

Tom Burwell, Madasamy Thangamuthu,* Jesum Alves Fernandes and Andrei N. Khlobystov*

Electrochemical CO_2 reduction reaction (eCO_2RR) provides a promising route for converting CO_2 into fuels and chemical feedstocks using renewable electricity. However, the dynamic nature of catalyst surfaces under reaction conditions complicates the identification of active sites and reaction intermediates, posing a major challenge for the rational design of efficient catalysts. *In situ* and *operando* characterisation techniques have therefore emerged as essential tools for directly probing catalyst behaviour under working electrochemical conditions. In this review, we present a unified perspective that integrates spectroscopy and microscopy techniques to correlate reaction intermediates, catalyst electronic structure evolution, and catalyst restructuring during eCO_2RR. Spectroscopic approaches, including surface-enhanced Raman spectroscopy (SERS), attenuated total reflection Fourier transform infrared spectroscopy (ATR-FTIR), and X-ray absorption spectroscopy (XAS), enable direct identification of key reaction intermediates and electronic structure changes during eCO_2RR. Complementarily, *in situ* microscopy techniques such as electrochemical atomic force microscopy (EC-AFM), electrochemical scanning tunnelling microscopy (EC-STM), and liquid-cell transmission electron microscopy (EC-TEM) reveal dynamic restructuring of the catalyst surface at the nanoscale and atomic scale. By bridging molecular-level intermediate identification with nanoscale structural evolution, this review highlights how dynamic catalyst behaviour governs activity and selectivity, providing new insight into the identification of true active phases. This integrated framework offers emerging strategies for rational catalyst design toward stable and selective CO_2 reduction catalysts.

Received 16th March 2026,
Accepted 19th May 2026

DOI: 10.1039/d6cc01583b

rsc.li/chemcomm

1. Introduction

The continuous rise in atmospheric CO_2 concentration driven by fossil-fuel combustion and industrial processes is one of the defining challenges of the 21st century.[1] Carbon capture and utilisation (CCU) offers a pathway to mitigate emissions while creating economic value by transforming CO_2 into fuels and chemical feedstocks such as CO, formate, methanol and hydrocarbons.[2] Unlike carbon capture and storage, which merely delays emissions, CCU enables a circular carbon economy aligned with global net-zero ambitions.[3] Among CCU strategies, the electrochemical CO_2 reduction reaction (eCO_2RR) is uniquely positioned to integrate with renewable electricity infrastructure. It operates under mild conditions, allows precise control over reaction potential and current, and is compatible with decentralised and modular reactor designs.[4]

School of Chemistry, University of Nottingham, University Park, Nottingham, NG7 2RD, UK. E-mail: madasamy.thangamuthu1@nottingham.ac.uk, andrei.khlobystov@nottingham.ac.uk

However, eCO_2RR is intrinsically complex. The thermodynamic stability of linear CO_2, the multiplicity of competing proton-electron transfer pathways, and the hydrogen evolution reaction (HER) collectively challenge catalyst selectivity and efficiency.[5] Addressing these challenges requires catalysts that lower activation barriers and direct complex reaction networks toward desired products under sustained operation.

1.1. Catalytic CO_2 conversion approaches

CO_2 can be converted through thermocatalytic, photocatalytic, photoelectrochemical (PEC), and electrochemical pathways. Thermocatalytic routes such as the Reverse Water–Gas Shift Reaction (RWGS)[6,7] (eqn (1)) and Fischer–Tropsch synthesis (eqn (2))[8,9] are industrially established but energy-intensive and reliant on externally supplied H_2. Photocatalytic and PEC systems integrate light harvesting with catalysis, but are often limited by poor quantum efficiencies, catalyst instability and scalability challenges.[10,11]

$$CO_2 + H_2 \rightarrow H_2O + CO \quad (1)$$

$$nCO + (2n + 1)H_2 \rightarrow C_nH_{2n+2} + nH_2O \quad (2)$$

In contrast, eCO_2RR decouples light absorption from catalysis, allowing direct utilisation of renewable electricity with flexible operational control. The key challenge lies not in proof-of-concept activity, but in achieving catalyst systems that combine high current density, a narrow product selectivity window, and an understanding of the dynamic restructuring under reaction conditions.[12] Recent advances in catalyst design, reaction engineering, and mechanistic understanding have further accelerated progress in eCO_2RR, as highlighted in recent reports.[13,14]

1.2. Electrochemical CO_2 conversion: pathways and selectivity

eCO_2RR proceeds *via* coupled proton–electron transfer steps at the cathode, producing a wide range of C_1 and C_{2+} products, including CO, formate, hydrocarbons and alcohols.[15] Product distribution is strongly governed by the catalyst composition, electronic structure, and local reaction environment.[4] Representative half-reactions and equilibrium potentials are summarised in Table 1.

The first electron transfer to CO_2, forming the unstable $CO_2^{\bullet-}$ radical, requires a potential of approximately −1.90 V *vs.* SHE at neutral pH, highlighting the need for catalysts that stabilise early intermediates and reduce kinetic barriers.[16] Under cathodic bias, the potential for CO_2 reduction overlaps with that of the HER, resulting in competition for active sites and electrons. Consequently, suppressing HER while promoting selective CO_2 conversion remains a central catalyst design objective.

Strategies such as modifying the electrolyte composition or employing aprotic media can reduce proton availability and suppress HER; however, such approaches often favour less-hydrogenated products (*e.g.*, CO or formate) over multi-proton pathways toward alcohols or hydrocarbons. Thus, catalyst design must ultimately be rooted in controlling intermediate binding energetics and surface reaction pathways.

Table 1 Representative C_1 and C_{2+} products of electrochemical CO_2 reduction, together with their standard equilibrium potentials and corresponding half-reactions

Electrons	CO_2 reduction half equation	Equilibrium potential (V *vs.* SHE at pH 7)
1	$CO_2 + e^- \rightleftharpoons CO_2^{\bullet-}$	−1.90
2	$CO_2 + 2H^+ + 2e^- \rightleftharpoons HCOOH$	−0.610
2	$CO_2 + 2H^+ + 2e^- \rightleftharpoons CO + H_2O$	−0.530
4	$CO_2 + 4H^+ + 4e^- \rightleftharpoons HCHO + H_2O$	−0.480
6	$CO_2 + 6H^+ + 6e^- \rightleftharpoons CH_3OH + H_2O$	−0.380
8	$CO_2 + 8H^+ + 8e^- \rightleftharpoons CH_4 + 2H_2O$	−0.240
12	$2CO_2 + 12H^+ + 12e^- \rightleftharpoons C_2H_4 + 4H_2O$	−0.349
12	$2CO_2 + 12H^+ + 12e^- \rightleftharpoons C_2H_5OH + 3H_2O$	−0.329
14	$2CO_2 + 14H^+ + 14e^- \rightleftharpoons C_2H_6 + 4H_2O$	−0.270
18	$3CO_2 + 18H^+ + 18e^- \rightleftharpoons C_3H_7OH + 5H_2O$	−0.310

1.3. Catalyst classification and descriptor framework

Electrocatalysts for eCO_2RR can be classified according to (i) product selectivity, (ii) composition, and (iii) structural complexity. These classifications provide a practical framework for correlating material identity with intermediate stabilisation and reaction outcomes.

From a product perspective, catalysts typically fall into three subcategories: (1) C_1-selective catalysts that predominantly produce CO or formate, (2) multicarbon (C_{2+}) catalysts that enable C–C coupling, and (3) materials dominated by HER. Most transition and p-block metals exhibit C_1 selectivity, while

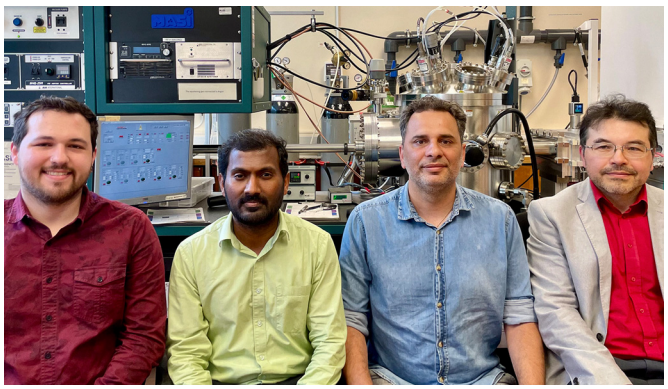

From left to right: Tom Burwell, Madasamy Thangamuthu, Jesum Alves Fernandes and Andrei N. Khlobystov

Tom Burwell is a KTP research associate specialising in electrocatalysis. His current research focuses on transforming lab-scale hydrogen production to an industrial scale. He received his PhD from the University of Nottingham on the electrochemical reduction of CO_2. His research interests include sustainable electrocatalysis and green fuel production.

Madasamy Thangamuthu is a Research Fellow in Electrocatalysis. His research interests focus on sustainable energy production technologies, specifically in photocatalysis, electrocatalysis and photoelectrocatalysis. He focuses on key areas such as green hydrogen production, CO_2 conversion into sustainable fuels and high-value chemicals, and green ammonia synthesis using readily available resources like water and solar energy.

Jesum Alves Fernandes is an Associate Professor of Chemistry. His research focuses on metal clusters for sustainable ammonia synthesis and hydrogen production. He developed the concept of on-surface atom assembly for heterogeneous catalyst production and used correlative spectroscopy, microscopy, and mechanistic modelling to identify key descriptors of catalytic reactions.

Andrei N. Khlobystov is a Professor of Nanomaterials. He develops electron microscopy as a tool for chemical discovery. He has created methods for imaging chemical reactions at the single-molecule level in real time, deriving reaction parameters like reaction rates and activation energy from the images. Recently, he has used identical-location electron microscopy to unravel the dynamics of individual particles in catalysis.

copper (Cu) uniquely facilitates substantial C_{2+} hydrocarbons and oxygenates formation (Fig. 1a). This product-based classification reflects the differences in *CO surface coverage and the ability to stabilise C–C coupling intermediates.

From a compositional viewpoint, catalysts include metallic systems (*e.g.*, Cu, Ag, Au, Sn, Bi),[17] oxide-derived materials,[18] bimetallic alloys,[19] molecular and M–N–C single-site catalysts, and hybrid metal–support architectures.[20] Alloying, heterostructuring, and defect engineering introduce additional electronics and geometric tuning parameters, enabling modulation of adsorption energetics and interfacial activity.

Structurally, catalysts may also be sub-categorised based on dimensionality and dispersion, including bulk foils, nanoparticles, nanoclusters, single atoms, and defect-engineered surfaces.[21] While nanoscale systems maximise active site utilisation, they are often dynamically unstable under reaction conditions, undergoing dissolution, redeposition, or phase transformation. As a result, the as-synthesised structure frequently differs from the true active phase.

These classifications converge within a descriptor-based framework linking adsorption energetics to selectivity. Catalytic performance is governed by the adsorption energetics of key intermediates such as *COOH, *OCHO, *CO and *H. A Volcano-type relationship linking intermediate binding energy to partial current density (Fig. 1b and c) illustrates how catalysts positioned within optimal energetic windows achieve high selectivity while suppressing competing pathways.[22] Thus, catalyst classification is inherently mechanistic, linking material structure to the energetic landscape of CO_2 reduction.[23,24] The interplay between descriptor energetics, catalyst surface dynamics, and resulting product selectivity is summarised schematically in Fig. 1d. This descriptor framework underpins the discussions in subsequent sections and motivates the need for direct mapping of catalyst behaviour under operating conditions. A brief comparison of major electrocatalyst classes, including their representative systems, product selectivity, and key advantages and limitations, is summarised in Table 2, providing a practical framework for catalyst selection and design.

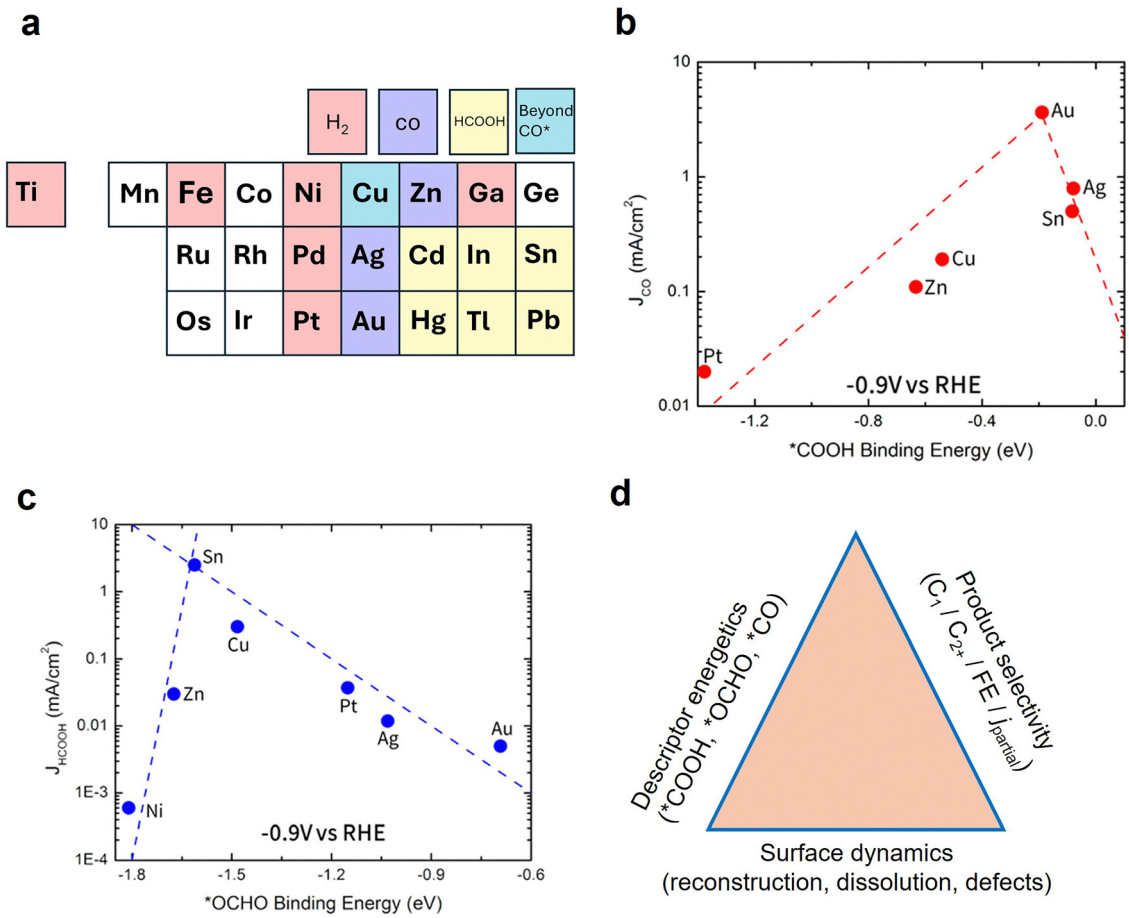

Fig. 1 (a) Table of d-block transition metals and p-block metalloids and their selectivity in the eCO_2RR. Reproduced from ref. 25 under CC-BY license. (b) Partial current density for CO formation (J_{CO} at −0.9 V *vs.* RHE) plotted as a function of *COOH binding energy for representative metal catalysts. (c) Partial current density for formate production (J_{HCOOH} at −0.9 V *vs.* RHE) plotted against *OCHO binding energy, showing a distinct volcano-type relationship with Sn positioned near the activity maximum due to near-optimal stabilisation of the *OCHO intermediate. Dashed lines serve as guides to the eye. Adapted from ref. 22 with permission from American Chemical Society, Copyright 2017. (d) Conceptual framework illustrating the interplay between descriptor-based intermediate binding energetics, dynamic surface evolution under reaction conditions, and resulting product selectivity in eCO_2RR.

1.4. Why *in situ* and *operando* mapping is essential

Descriptor-based volcano plots provide valuable thermodynamic insight but represent static energetic landscapes. In practice, catalyst surfaces evolve continuously under applied bias, undergoing oxidation–reduction cycling, defect formation, dissolution–redeposition, electrolyte-induced restructuring, and intermediate accumulation.[23,24] These dynamic processes can shift adsorption energetics and alter selectivity in real time. *In situ* and *operando* mapping is therefore essential to bridge the gap between idealised binding-energy descriptors and the behaviour of working catalysts. By simultaneously tracking surface intermediates, electronic structure, and morphological evolution, *in situ* and *operando* techniques enable identification of transient active states and correlation with product distribution. Understanding how catalysts dynamically enter or depart from optimal binding-energy windows is critical for designing systems that remain selective and stable under realistic operating conditions.

Despite the rapid growth of *in situ* and *operando* studies in eCO_2RR, existing review articles have predominantly focused on either individual spectroscopic techniques (*e.g.*, infrared (IR), Raman, and X-ray absorption spectroscopy (XAS)-based studies)[26–28] or specific catalyst systems such as Cu-based catalysts and single-atom catalysts,[29–31] often treating intermediate identification and catalyst restructuring as separate aspects. However, catalytic performance in eCO_2RR emerges from the dynamic interplay between reaction intermediate formation and the catalyst's electronic structure evolution, and morphological transformation under operating conditions. In this review, we address this gap by integrating spectroscopy and microscopy insights within a unified framework that directly links molecular-scale intermediates to nanoscale structural evolution. By systematically correlating these processes, we provide a comprehensive understanding of how dynamic catalyst behaviour governs activity and selectivity, thereby offering a more complete mechanistic picture complementing previously reported reviews.

It is important to distinguish between *in situ* and *operando* characterisation, as these terms are often used interchangeably in the literature. *In situ* techniques refer to measurements performed under controlled reaction-relevant conditions, such as applied potential, electrolyte environment, or gas atmosphere, enabling observation of catalyst behaviour under conditions that approximate those of catalysis. In contrast, *operando* techniques involve simultaneous measurement of catalyst structure or reaction intermediates together with catalytic performance metrics, such as current density or product selectivity, thereby enabling direct correlation between observed species and catalytic function. In this review, we adopt this distinction to differentiate studies that directly link structural or spectroscopic observations with catalytic activity from those that probe catalyst behaviour under reaction-relevant conditions without simultaneous performance correlation.

2. Elucidating eCO_2RR intermediates *via in situ/operando* spectroscopy

Achieving high FE, industrially relevant current densities and long-term durability remain a central challenge in eCO_2RR. While descriptor-based frameworks provide valuable thermodynamic guidance for catalyst design, real catalytic surfaces often undergo dynamic restructuring under operating conditions, leading to transient active states that cannot be captured by *ex situ* characterisation alone. Consequently, *in situ* and *operando* techniques have become indispensable for elucidating reliable structure–function relationships that govern eCO_2RR performance.

Spectroscopic methods provide direct insight into reaction intermediates and the electronic structure of catalysts during catalysis. Vibrational spectroscopies such as surface-enhanced Raman spectroscopy (SERS) and attenuated total reflectance Fourier transform infrared spectroscopy (ATR-FTIR) enable direct identification of surface-bound intermediates, including *COOH, *OCHO, *CO and *H, providing molecular-level information on reaction pathways and product selectivity. Complementarily, XAS offers element-specific information on oxidation state, local coordination environment and electronic structure, allowing real-time tracking of catalyst reconstruction and dynamic active-phase formation during eCO_2RR.

Together, these spectroscopic approaches enable experimental validation of key intermediates predicted by theoretical

Table 2 Classification of eCO_2RR catalysts based on their typical products, comparing advantages and limitations

Catalyst Class	Examples	Main products	Advantages	Limitations
Noble metals	Au, Ag, Pd	CO	High selectivity; low overpotential	Expensive; limited multi-carbon products
Post-transition/main group metalloids	Sn, Bi, In	Formate	High FE; suppresses HER	Limited products; low current density; high overpotential
Cu-based	Cu, Cu oxides	C_{2+} products (ethylene, ethanol)	Unique C–C coupling ability; broad product range	Poor stability; dynamic restructuring; mixed selectivity
Bimetallic/alloys	Cu–Ag, Cu–Pd	Tunable (CO, C_{2+})	Synergistic effects; tunable binding energies and selectivity	Complex synthesis; difficult to control active sites
M–N–C	Fe–N–C, Co–N–C	CO	High density of atomically dispersed active sites	Poor stability; limited C_{2+} formation
Molecular catalysts	Metal-phthalocyanines (CoPc, FePc, NiPc)	CO/formate	Tunable coordination environment; well-defined active sites	Limited stability; degradation under electrochemical conditions

models and reveal how catalyst electronic structure evolves during CO_2 reduction. In this section, we highlight recent advances in vibrational and X-ray spectroscopies that provide mechanistic insight into intermediate formation, catalyst transformation, and reaction pathways in eCO_2RR systems.

2.1. Surface-enhanced Raman spectroscopy (SERS)

SERS has emerged as a powerful *in situ* and *operando* tool for resolving the vibrational fingerprints of reaction intermediates adsorbed on catalyst surfaces during eCO_2RR. By exploiting plasmonic enhancement at roughened metal interfaces, SERS enables detection of transient, low-coverage species that are otherwise inaccessible to conventional Raman spectroscopy. Early landmark work by Chernyshova *et al.* employed SERS on roughened Cu electrodes to assign potential-dependent vibrational bands to key intermediates, including $CO_2^{\bullet-}$ and CO in distinct binding configurations (Fig. 2a).[32] A characteristic CO stretching band emerged at potentials more negative than −0.9 V *vs.* Ag/AgCl, accompanied by a redshift with increasing overpotential, consistent with strengthened chemisorption at Cu active sites. These observations directly demonstrated the sensitivity of CO binding configuration and surface coverage to applied potential. A vibrational feature of particular mechanistic significance is the transient band near 1540 cm^{-1}, attributed to the $CO_2^{\bullet-}$ intermediate. This signal, correlated with a low-frequency mode at ~350 cm^{-1}, disappears at more cathodic potentials, suggesting either diminished surface coverage or shortened lifetime of $CO_2^{\bullet-}$ under strongly reducing conditions. The loss of this signal coincides with increasing CO-related features, supporting a mechanistic transition in which surface-bound CO becomes the dominant intermediate at higher overpotentials. The increased surface coverage of *CO at more negative potentials correlates with CO being the dominant reduction product on the Cu electrode, highlighting how potential-dependent intermediate stabilisation influences eCO_2RR selectivity.

Beyond identification of intermediates, SERS has enabled quantitative insight into surface coverage dynamics. Zhan *et al.* monitored Cu–CO interactions under *operando* conditions and identified two distinct vibrational modes: a stretching mode (P1) at ~280 cm^{-1} and a rotational mode (P2) at 355–370 cm^{-1} (Fig. 2b and c).[33] The intensity ratio (P2/P1) followed Langmuir-type adsorption behaviour (Fig. 2d) and served as a quantitative descriptor of CO surface coverage. Notably, this spectroscopic parameter correlated directly with FE for C_{2+} products (Fig. 2e and f), indicating that increased *CO accumulation promotes C–C coupling and enhances multicarbon product formation. Building on this concept of spectroscopic descriptors, Chen *et al.* further demonstrated that the intensity ratio between Raman bands corresponding to linearly adsorbed ($*CO_{atop}$) and bridge-bound ($*CO_{bridge}$) configurations can be used to predict product selectivity.[34] By correlating this SERS-derived ratio with catalytic performance, the authors showed that a higher relative population of $*CO_{bridge}$ favours ethanol formation, as this configuration stabilises *CO–CO coupling and oxygenated intermediates, whereas dominant $*CO_{atop}$ configurations are associated with ethylene production through more direct C–C coupling and subsequent hydrogenation pathways. This finding highlights the potential of *in situ* SERS to provide quantitative descriptors linking intermediate surface coverage with catalytic selectivity and enabling mechanistically informed catalyst screening.

SERS has also provided insight into bimetallic synergy. Gao *et al.* demonstrated that incorporating Ag into Cu surfaces promotes a CO spillover mechanism, whereby CO generated on Ag sites migrates to neighbouring Cu domains, increasing the local *CO surface coverage on Cu and thereby promoting C–C coupling. This tandem Ag–Cu catalyst achieved a FE of ~76% for C_{2+} products, with ethylene as the dominant product.[35] *In situ* Raman spectra revealed intensified C–H vibrational features upon Ag incorporation, indicative of increased surface populations of hydrogenated intermediates such as *CHO, $*CH_3$, and $*C_2H_2$. The formation of these intermediates reflects enhanced hydrogenation of coupled *CO species on Cu sites, consistent with reaction pathways leading predominantly to ethylene formation *via* CO dimerisation (OCCO) followed by proton–electron transfer steps.

Collectively, these studies illustrate that SERS not only enables the identification of transient intermediates but also provides quantitative descriptors that link molecular-scale surface coverage to macroscopic catalytic performance. Fig. 3 summarises characteristic vibrational signatures reported for key eCO_2RR intermediates across catalyst systems, offering a consolidated framework for peak assignment and mechanistic interpretation.

2.2. Attenuated total reflectance Fourier transform infrared spectroscopy (ATR-FTIR)

Complementary to SERS, *in situ* ATR-FTIR and its surface-enhanced variant (ATR-SEIRAS) provide direct detection of polar surface-bound intermediates during eCO_2RR, including *COOH, *OCHO, *CHO and other hydrogenated species. Owing to its sensitivity to dipole-active vibrational modes, ATR-FTIR is particularly powerful for tracking potential-dependent evolution of reaction pathways and distinguishing competing reduction channels. For example, Wang *et al.* employed ATR-FTIR to investigate the size-dependent reactivity of Cu quantum dots (Fig. 4a–d).[36] This study revealed a strong correlation between applied potential and the emergence of intermediates such as *COOH, *COCHO and *CHO. Notably, decreasing nanoparticle size enhanced overall eCO_2RR activity and promoted C–C coupling, achieving an ethylene FE of 81.5%. This selectivity shift was accompanied by a pronounced increase in a vibrational band at ~1145 cm^{-1}, assigned to C–C coupled intermediates, directly linking nanoparticle size to intermediate stabilisation and multicarbon formation.

ATR-FTIR has also elucidated how electronic structure modification alters reaction pathways. Liu *et al.*[37] demonstrated that sulfur-doped Cu nanosheets (Cu NSs) prepared *via* vulcanisation selectively produced formate as the sole liquid product with a FE of 82% at 250 mA cm^{-2}. *In situ* ATR-FTIR measurements showed preferential stabilisation of the HCOO*

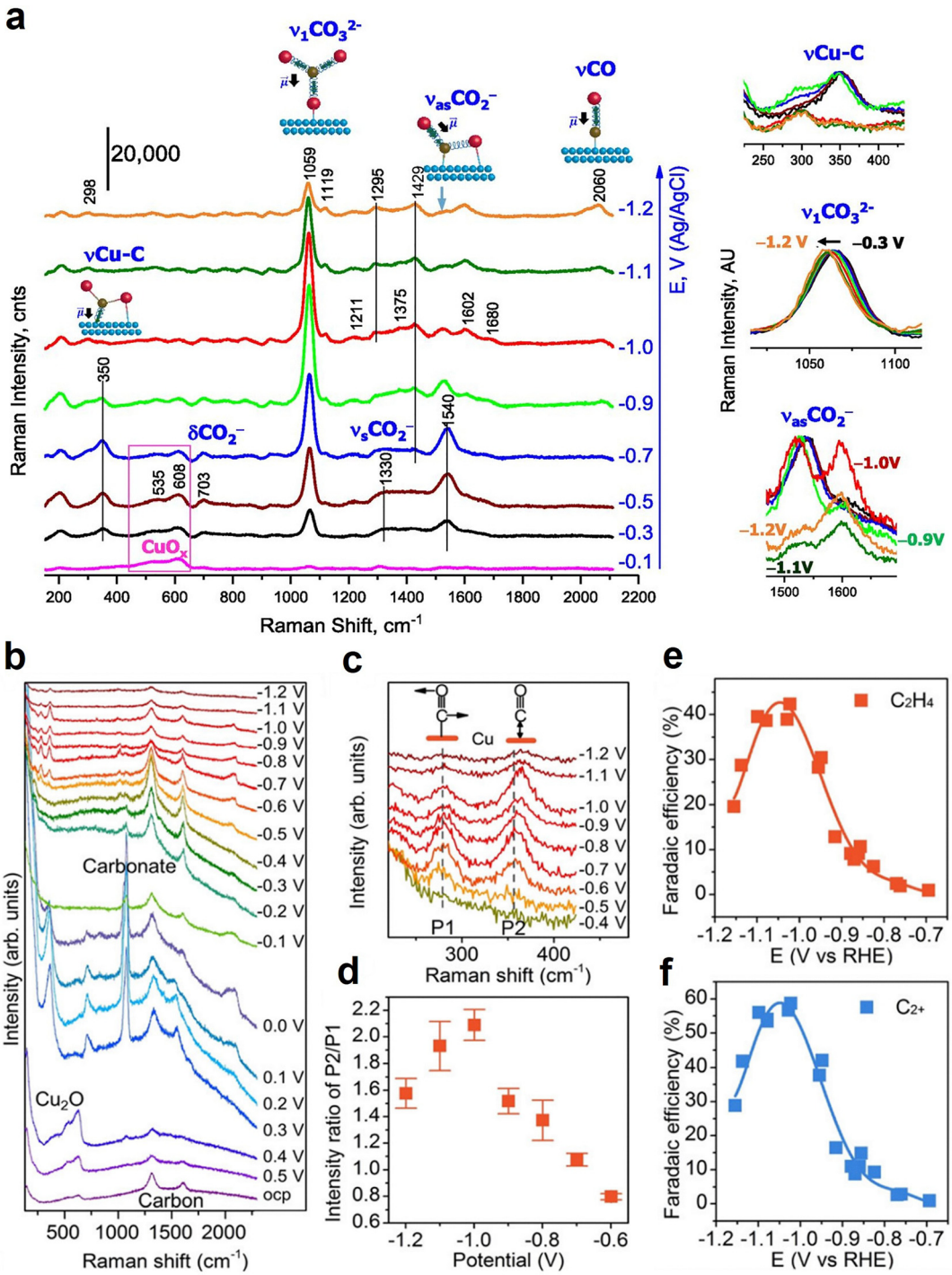

Fig. 2 (a) *In situ* SERS of roughened Cu foil in CO_2-saturated 0.1 M $NaHCO_3$, with potential as a function of Raman shift, with labelled intermediates and their expected vibrational shifts. Adapted from ref. 32 with permission from National Academy of Sciences, Copyright 2018. (b) Raman spectra from OCP to −1.2 V *vs*. RHE, (c) Inset of zoomed-in spectra of P1 and P2 from −0.4 to −1.2 V *vs*. RHE and (d) Ratio of P2 to P1 as a function of potential, (e) FE of C_2H_4 as a function of potential, (f) FE of C_{2+} products as a function of potential. Adapted from ref. 33 under CC-BY license.

intermediate upon sulfur incorporation (Fig. 4e–g), fundamentally redirecting the reaction pathway compared to undoped Cu systems. These results highlight how heteroatom doping can tune intermediate binding energetics and suppress competing hydrogenation routes.

Beyond intermediate identification, ATR-FTIR has also provided insight into how catalyst reconstruction under reaction conditions influences product selectivity and catalytic performance. Delmo *et al.* showed that pre-anodisation of Cu catalysts generates subsurface oxide species that significantly

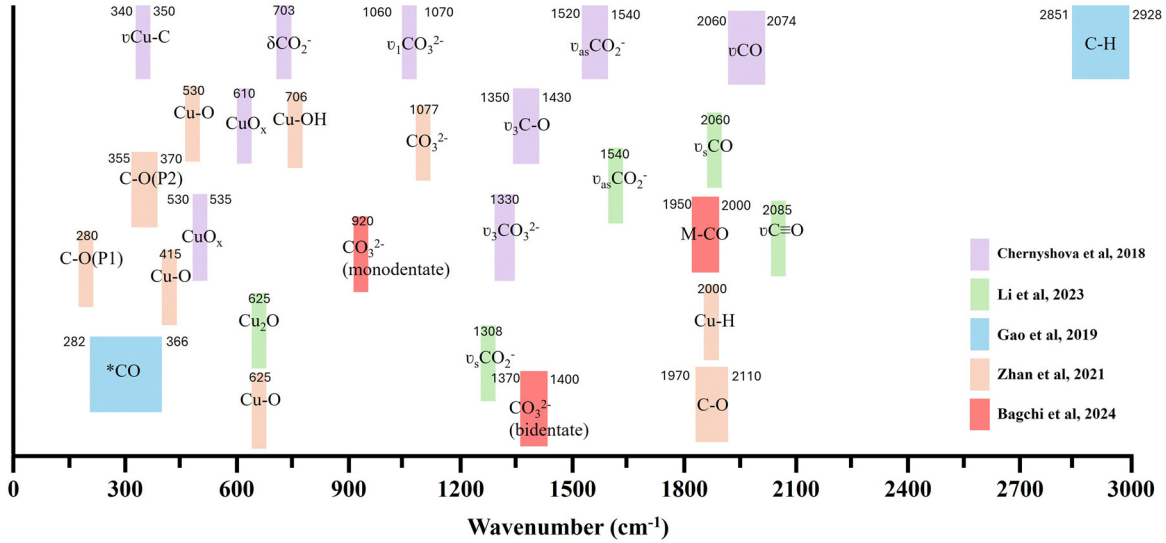

Fig. 3 Commonly observed *in situ* SERS peaks in eCO_{2RR} and corresponding surface species attributed to them.

enhance C–C coupling during CO_2 electroreduction.[38] *In situ* ATR-FTIR measurements revealed stronger signals corresponding to CO-related intermediates, indicating increased *CO surface coverage on oxide-derived Cu. This pre-anodised Cu catalyst produced C_{2+} products including ethylene and ethanol, whereas the as-prepared Cu film predominantly resulted in C_1 products. It demonstrates that subsurface oxygen stabilises *CO intermediates and facilitates CO dimerisation to the OCCO species, a key step in multicarbon formation.

Similarly, Liang *et al.* reported that $BiPO_4$ undergoes an *in situ* transformation to $Bi_2O_2CO_3$ during CO_2 reduction, as evidenced by ATR-FTIR measurements (Fig. 4h).[39] The spectra revealed strong vibrational bands associated with *OCHO intermediates, indicating preferential stabilisation of this species on the reconstructed surface. As a result, the catalyst exhibited high selectivity toward formate with FE approaching 100%, demonstrating that the $Bi_2O_2CO_3$ phase promotes the two-electron reduction pathway by stabilising the *OCHO intermediate while suppressing competing hydrogen evolution and C–C coupling pathways.

Taken together, these studies demonstrate that ATR-FTIR not only enables identification of key reaction intermediates but also captures dynamic catalyst reconstruction and pathway switching under applied bias. By correlating vibrational signatures with applied potential, nanoparticle size, doping chemistry and phase transformation, ATR-FTIR serves as a critical bridge between molecular-level intermediate stabilisation and macroscopic catalytic performance.

2.3. X-ray absorption spectroscopy (XAS) and electronic structure probing

XAS, encompassing both X-ray absorption near-edge structure (XANES) and extended X-ray absorption fine structure (EXAFS), has become an indispensable technique for probing the electronic and local atomic structure of CO_2RR electrocatalysts under working conditions.[40] By tracking oxidation state changes, coordination environment variations, and bond distances in real time, XAS yields direct insight into the active site nature and dynamic structural evolution that accompany catalytic activity, information that is difficult to obtain *via* purely *ex situ* methods.[41] Studies leveraging XAS have revealed how subtle electronic and coordination changes correlate with product selectivity and reaction pathways, providing a molecular-level link between catalyst structure and catalytic function.

In Cu-based eCO_2RR catalysts, XAS has played a pivotal role in revealing how electronic structure and oxidation state evolve dynamically under reaction conditions and correlate with product selectivity. For instance, Lin *et al.* employed seconds-resolved *operando* XAS to track the chemical-state evolution of oxide-derived Cu electrocatalysts during eCO_2RR, revealing that under cathodic bias the catalyst stabilises in a mixed valence state consisting of approximately equal proportions of $Cu^{(0)}$ and $Cu^{(I)}$ (Fig. 5a), rather than converting completely to metallic Cu.[42] This dynamic $Cu^{(I)}/Cu^{(0)}$ interface was associated with enhanced formation of C_2 oxygenates, particularly ethanol, reaching a FE of ~13% at −0.75 V under optimised conditions. XAS analysis suggested that $Cu^{(I)}$ species stabilise key *CO and *CO–CO intermediates, while adjacent metallic $Cu^{(0)}$ sites facilitate electron transfer and hydrogenation steps. The coexistence of $Cu^{(I)}$ and $Cu^{(0)}$ therefore promotes *CO dimerisation and subsequent hydrogenation toward ethanol, demonstrating that dynamic mixed-valence active sites govern C–C coupling pathways and product selectivity rather than a purely metallic Cu surface.

Complementarily, Feijóo *et al.* employed *in situ* XAS to continuously monitor oxidation state and coordination number changes in 5 nm Cu nanoparticles during eCO_2RR (Fig. 5b and c).[43] The measurements revealed progressive ligand desorption and restructuring of the nanoparticles into under-coordinated metallic Cu nanograins, accompanied by an increase in Cu–Cu coordination number during electrocatalysis. These

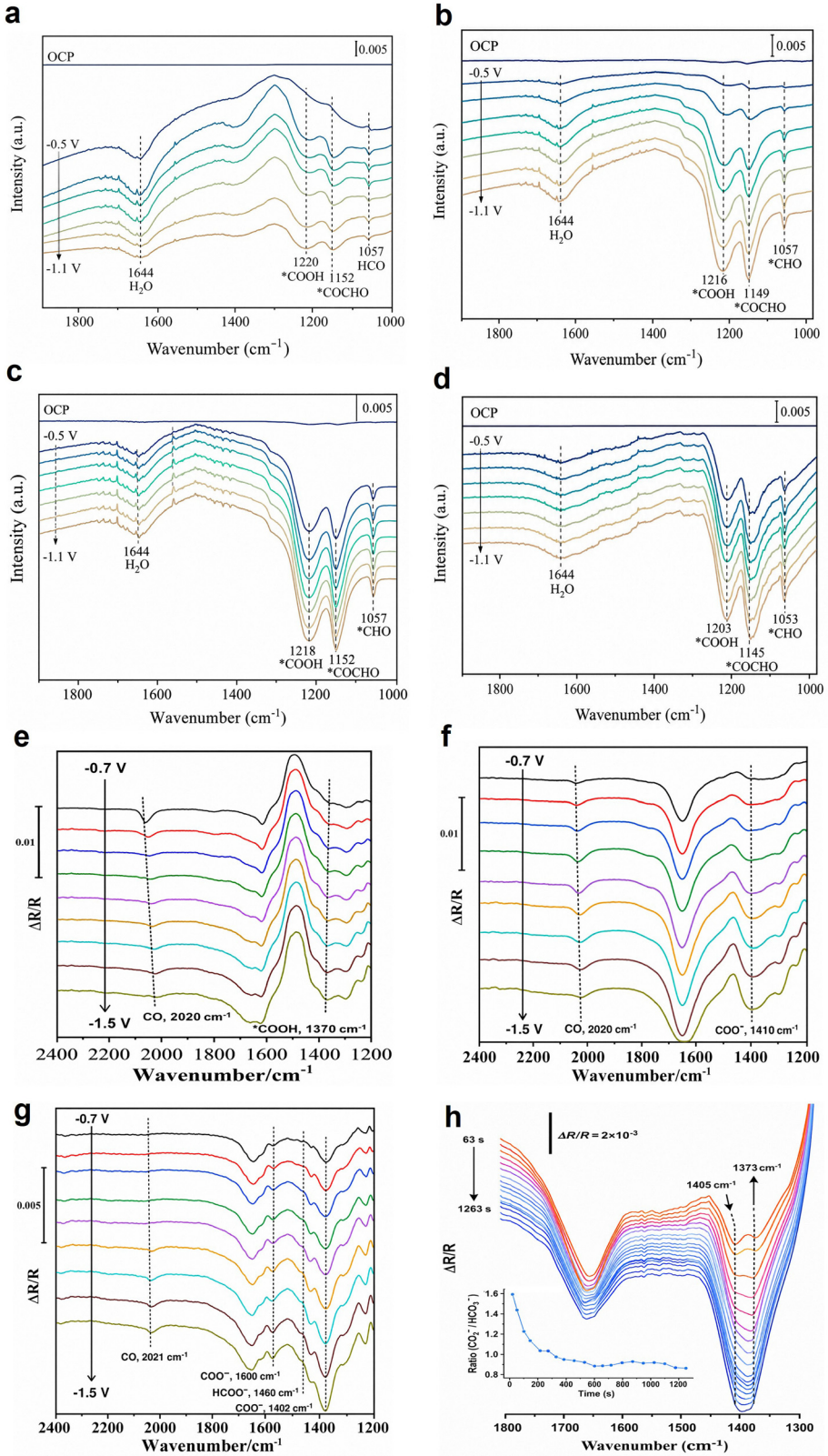

Fig. 4 *In situ* ATR-FTIR of the various Cu quantum dot sizes under varying applied potentials: (a) Cu-50 nm, (b) Cu-25 nm, (c) Cu-15 nm, (d) Cu-5 nm. Adapted from ref. 36 with permission from Wiley-VCH, Copyright 2024. *In situ* ATR-FTIR of (e) Cu NSs, (f) Cu + S NSs, (g) Cu_2S/C. Adapted from ref. 37 with permission from the Royal Society of Chemistry, Copyright 1996. (h) *In situ* time-resolved ATR-IR spectra of CO_2RR recorded at −0.6 V for $BiPO_4$ nanoparticles in the CO_2-saturated 0.5 M $KHCO_3$ electrolyte. Adapted from ref. 39 with permission from Elsevier, Copyright 2023.

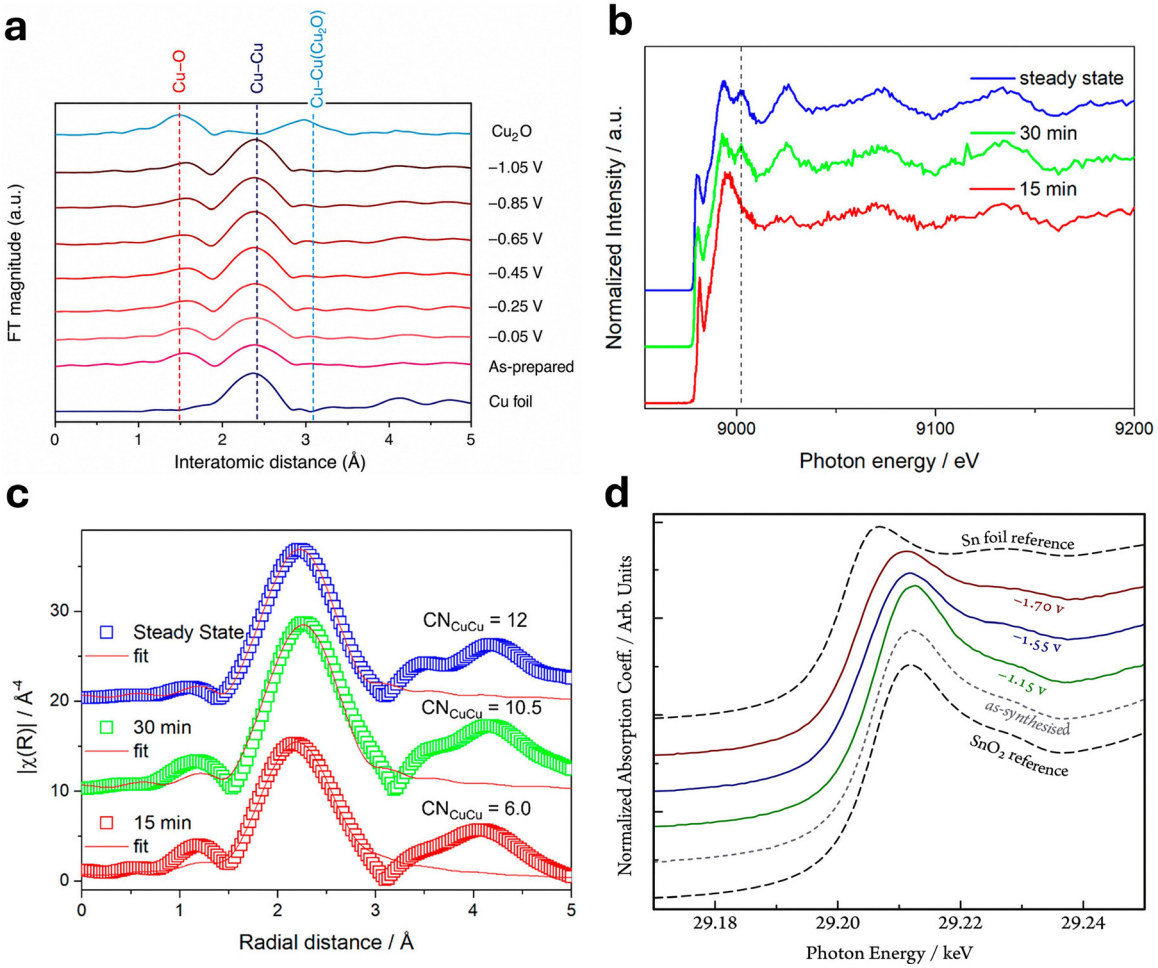

Fig. 5 (a) Potential dependence of *operando* EXAFS spectra of the CuO_x under eCO_2RR in 0.5 M CO_2-saturated $KHCO_3$ using chronoamperometry. Adapted from ref. 42 under the CC-BY license. (b) Full XAS spectra after different times of electrolysis with dashed lines showing a metallic Cu feature at ~9002 eV emerging under eCO_2RR, (c) the Cu–Cu coordination number (CN) of metallic Cu increases throughout the dynamic evolution of the catalyst from 6.0 after 15 min to 10.5 after 30 min to 12.0 after 1 h. Adapted from ref. 43 with permission from the American Chemical Society, Copyright 2023. (d) Sn K-edge XANES of the SnO_2 NPs@rGO catalyst acquired at different electrode potential values (marked in the figure *vs.* Ag/AgCl). Spectra of pure SnO_2, pure metallic Sn, and as-synthesised SnO_2 NPs@rGO, measured at the same beam-line under identical conditions, are also plotted as a reference. Adapted from ref. 44 with permission from Elsevier, Copyright 2018.

dynamically generated low-coordination Cu sites were identified as the catalytically active surface responsible for C–C coupling. Under reaction conditions, the catalyst achieved a FE of ~35% for ethylene as the dominant product. It suggested that the under-coordinated Cu sites enhance the adsorption of *CO intermediates and facilitate their dimerisation to *OCCO, a key step toward multicarbon formation. These findings demonstrate that dynamic restructuring of Cu nanoparticles into low-coordination metallic domains governs C–C coupling activity and ethylene selectivity during eCO_2RR.

In p-block catalysts such as Sn- and Bi-based materials, *in situ* investigations have elucidated how dynamic changes in oxidation state and local coordination influence formate selectivity by stabilising *OCHO-type intermediates. Tin oxide (SnO_2) nanoparticle catalysts also undergo potential-dependent reduction during eCO_2RR, as revealed by XAS. Dutta *et al.* observed progressive reduction of Sn^{4+} to mixed SnO_x species and eventually to metallic Sn at increasingly cathodic potentials (Fig. 5d).[44] Spectroscopic analysis showed that partially reduced SnO_x species containing Sn^{2+} stabilise OCHO intermediates, promoting the two-electron reduction of CO_2 to formate. Under these conditions, formate remains the dominant product at potentials up to approximately −1.1 V *vs.* Ag/AgCl, whereas further reduction of the catalyst to metallic Sn shifts the reaction pathway toward hydrogen evolution, leading to a marked decrease in formate selectivity. These results demonstrate that maintaining mixed Sn oxidation states is critical for sustaining selective CO_2-to-formate conversion, highlighting the importance of *in situ* spectroscopy in identifying active catalytic states.

Bi-based catalysts exhibit analogous electronic structure evolution during CO_2 electroreduction. Zhao *et al.* employed synchrotron X-ray absorption spectroscopy together with *in situ* ATR-FTIR to probe the electronic and local coordination

environment of boron (B)-doped Bi catalysts.[45] XAFS analysis revealed B-induced modulation of Bi–Bi coordination and electronic structure, producing an electron-rich Bi surface that enhances CO_2 activation. ATR-FTIR measurements further identified the formation of the *OCHO intermediate ($\sim$1393 cm^{-1}) during CO_2 reduction, confirming the formate production pathway. The optimised B-doped Bi catalyst achieved a FE of 91.5% for formate at −1.1 V *vs.* RHE in an H-cell and up to 95% FE in a flow cell, while maintaining stable operation for 20 h at a current density of −190 mA cm^{-2}. These results demonstrate that electronic structure modulation of Bi centres promotes *OCHO stabilisation and accelerates charge-transfer kinetics, leading to highly selective and stable CO_2-to-formate conversion.

Together, these studies demonstrate that the active phase of p-block catalysts is not static but dynamically evolves under applied bias. *In situ* and *operando* XAS therefore provides direct mechanistic insight linking oxidation-state dynamics, intermediate stabilisation, and macroscopic formate selectivity.

XAS is particularly powerful for probing the dynamic coordination environment of atomically dispersed catalysts during CO_2 electroreduction. Martini *et al.* employed Co K-edge XANES to monitor structural evolution of Co–N–C single-atom catalysts during eCO_2RR (performed at −1.2 V *vs.* RHE in 0.1 M $KHCO_3$).[46] Time-resolved analysis revealed the coexistence of three cobalt species under reaction conditions: intact Co–N_4 moieties, partially reduced Co–Co aggregates, and a distorted Co–N_4 configuration coordinated with axial CO ligands, which was identified as the dominant active state for CO formation. EXAFS fitting and wavelet transform analysis further confirmed the emergence of Co–Co scattering contributions ($\approx$2.5 Å) associated with partial aggregation of single atoms, together with Co–N and Co–C coordination shells characteristic of the atomically dispersed environment. These observations indicate that adsorbate-induced distortion of the Co–N_4 site and metal–CO interactions stabilise key CO intermediates and promote selective CO production, whereas progressive aggregation into metallic Co clusters diminishes CO selectivity due to competing hydrogen evolution.

Overall, these observations establish that XAS bridges molecular-scale intermediate identification and mesoscale structural evolution by revealing how electronic structure and coordination environments evolve dynamically during eCO_2RR. When integrated with complementary techniques such as SERS and ATR-FTIR, XAS provides a comprehensive framework linking oxidation-state dynamics, active-site reconstruction, and catalytic performance. A summary of representative *in situ* and *operando* spectroscopic studies discussed in this review,

Table 3 Summary of *in situ* and *operando* spectroscopic studies revealing reaction intermediates and catalytic pathways in eCO_2RR

Technique	Ref.	Catalyst system	Measurement insight (*in situ*/*operando*)	Intermediate	Catalytic implication
SERS	Chernyshova *et al.*[32]	Roughened Cu electrode	*In situ*: Raman bands (1540 cm^{-1}, 350 cm^{-1}) reveal early CO_2 activation	$*CO_2^{\bullet-}$ *CO	Controls CO/formate selectivity
SERS	Zhan *et al.*[33]	Cu nanocubes	*Operando*: CO bands P1 (280–370 cm^{-1}) and P2 (1970–2110 cm^{-1}); P2/P1 intensity reflects high CO coverage	*CO	Promotes ethylene formation
SERS	Chen *et al.*[34]	Cu nanoparticles	*In situ*: Bands of *COOH (1042 cm^{-1}), *CO (2000–2100 cm^{-1}), $*CH_2CHO$ (530 cm^{-1}); K^+ increases CO coverage, promoting CO dimerisation	*COOH *CO $*CH_2CHO$	Ethylene and ethanol formation
SERS	Gao *et al.*[35]	Ag–Cu nanowires	*In situ*: CO generated on Ag spills over to Cu, increasing *CO coverage and enabling C–C coupling	*CO *CHO	C_{2+} products (76% FE)
ATR-FTIR	Wang *et al.*[36]	Cu quantum dots	*In situ*: Potential-dependent *COOH, *COCHO, *CHO band (1000–1250 cm^{-1}), decreasing the size promotes C–C coupling	*COOH *COCHO	Ethylene (81.5% FE)
ATR-FTIR	Liu *et al.*[37]	Cu_2S nanosheets	*In situ*: Strong $HCOO^-$ bands; suppressed COOH* pathway; heteroatom doping tunes intermediate binding	*OCHO, $*COO^-$	Formate (82% FE)
ATR-SEIRAS	Delmo *et al.*[38]	Oxide-derived Cu	*In situ*: Strong *CO uptake; bands at $\sim$1426 & 1327 cm^{-1}; Subsurface O promotes *CO + *CHO coupling	*CHO *COCHO	C_2 products (ethylene, ethanol)
ATR-FTIR	Liang *et al.*[39]	$Bi_2O_2CO_3$/Bi	*In situ*: $CO_3^{2-} \rightarrow HCO_3^-$ interfacial dynamics electrolysis; $Bi_2O_2CO_3$ phase promotes two-electron reduction	*OCHO	Formate (100% FE)
XAS	Lin *et al.*[42]	Cu nanocubes	*Operando*: Mixed Cu^0/Cu^+ promotes CO dimerisation	OCCO*	Ethanol (12% FE)
XAS	Feijóo *et al.*[43]	5 nm Cu nanoparticles	*In situ*: Cu_2O is reduced to low-coordinated Cu nanograins, promoting C-C coupling	*CO reservoir	Ethylene (35% FE)
XAS	Dutta *et al.*[44]	SnO_2 nanoparticle	*In situ*: SnO_x is reduced to Sn^{2+} and Sn^0; mixed oxidation states are crucial for formate selectivity	*OCHO	Formate pathway
XAFS	Zhao *et al.*[45]	B-doped Bi nanosheets	*In situ*: Electron-rich Bi stabilises *OCHO	*OCHO	Formate (95% FE)
XAS	Martini *et al.*[46]	Co–N–C single-atom catalyst	*In situ*: Co–N_4 and metal-CO interactions stabilise *CO intermediates	*CO	CO production

highlighting the intermediates identified and their relationship to catalytic performance, is provided in Table 3. Although the term *operando* is widely used in the literature, not all studies strictly meet the definition of simultaneous correlation between spectroscopic observations and catalytic performance. In many spectroscopic investigations of eCO_2RR, reaction intermediates, and catalyst electronic structure are probed under electrochemical conditions, while product quantification is performed separately, often using independent cells or periodic sampling techniques. As a result, such studies are more appropriately described as *in situ*, and the studies summarised here therefore include both *in situ* and *operando* investigations.

3. Visualising structural evolution of the catalyst *via in situ* microscopy

To elucidate the dynamic structural evolution of catalysts under eCO_2RR conditions, advanced microscopy techniques play a pivotal role. While spectroscopic methods provide insight into oxidation states and adsorbate interactions, *in situ* microscopy enables direct visualisation of catalyst restructuring under eCO_2RR conditions. Techniques such as electrochemical atomic force microscopy (EC-AFM), electrochemical scanning tunnelling microscopy (EC-STM), and electrochemical/identical location transmission electron microscopy (EC/IL-TEM) provide high-resolution, real-time visualisation of morphological and crystallographic transformations occurring under applied bias. During catalysis, catalysts frequently undergo significant structural changes, including surface roughening, defect generation, nanoparticle restructuring, aggregation, and phase transitions. These transformations are often closely correlated with variations in catalytic activity, product selectivity, and long-term stability. By directly capturing nanoscale surface dynamics at electrified interfaces, *in situ* microscopy provides critical insight into the evolution of active sites during eCO_2RR.

Together with spectroscopic techniques discussed in the previous section, these microscopic approaches establish a powerful framework for linking catalyst structure, dynamic surface evolution, and electrochemical performance. Such insights are essential for guiding the rational design and optimisation of next-generation catalysts for efficient and selective eCO_2RR.

3.1. Electrochemical-atomic force microscopy (EC-AFM)

EC-AFM is a powerful non-optical surface characterisation technique that enables nanoscale topographical imaging of electrode surfaces under applied bias. By scanning a cantilever-mounted probe in contact or tapping mode, EC-AFM provides real-time insight into surface roughening, nanoparticle formation, and morphological restructuring during electrochemical operation, without the need for vacuum-based electron microscopy.

Simon *et al.* employed EC-AFM to monitor the surface evolution of a Cu(100) thin film during electrochemical eCO_2RR (Fig. 6a–c).[47] AFM imaging revealed that even upon immersion of the catalyst into CO_2-saturated 0.1 M $KHCO_3$ at open-circuit potential (OCP), the initially atomically flat Cu terraces rapidly transformed into a roughened surface decorated with nanoparticulate and platelet-like features. This reconstruction was attributed to dissolution of the native Cu oxide layer followed by reprecipitation of Cu species, forming epitaxially aligned $Cu_2O(111)$ platelets on the Cu(100) surface. Upon applying cathodic potentials relevant to eCO_2RR (−0.5 to −1.1 V *vs.*

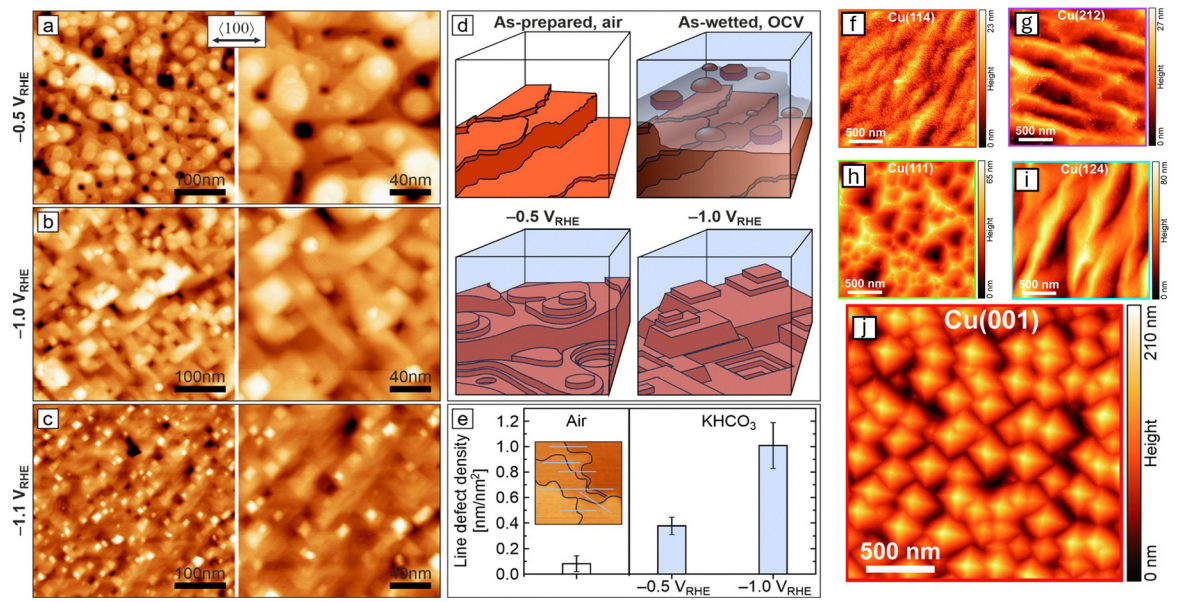

Fig. 6 AFM of Cu(100) film at (a) −0.5 V, (b) −1.0 V, (c) −1.1 V, *vs* RHE, (d) Schematics of morphologies observed, (e) line-defect densities from *in situ* AFM images. Adapted from ref. 47 under the CC-BY license. (f)–(j) AFM images under the pulse program of different Cu crystalline facets. Adapted with permission from ref. 48 under the CC-BY license.

RHE), the oxide layer rapidly reduces, and the surface evolves into potential-dependent morphologies characterised by mound–pit structures at −0.5 V and rectangular terraces with crystallographically aligned step edges at more negative potentials. These transformations increase the density of under-coordinated Cu step sites, which are widely recognised as favourable adsorption sites for CO intermediates and are implicated in facilitating C–C coupling pathways leading to C_2 products such as ethylene on Cu(100) surfaces. Although this EC-AFM study did not directly quantify catalytic performance metrics such as FE or product selectivity, the *in situ* observations demonstrate that potential-dependent surface reconstruction dynamically modifies the distribution of active sites, implying that catalytic behaviour during eCO_2RR is governed by the evolving surface structure rather than the static morphology of the as-prepared catalyst.

Building on these insights, Wang *et al.* employed identical-grain EC-AFM combined with EBSD to probe facet-dependent restructuring of polycrystalline Cu electrodes during eCO_2RR (Fig. 6f–j).[48] AFM under alternating anodic and cathodic pulses (+1.0 and −1.0 V *vs.* RHE) revealed pronounced facet-dependent surface reconstruction. Planar facets showed the strongest restructuring: Cu(001) evolved into square-based pyramidal structures reflecting four-fold symmetry, while Cu(111) formed triangular pits consistent with its three-fold lattice symmetry. In contrast, stepped facets such as Cu(114), Cu(212), and Cu(124) developed elongated or directionally oriented features. These morphological transformations increase the density of low-coordination surface sites that stabilise CO intermediates and facilitate C–C coupling. Electrocatalysis results showed that pristine Cu mainly produced formate (21.2%) and CO (6.5%) at −0.8 V *vs.* RHE, whereas more negative potentials promoted hydrocarbon formation, reaching CH_4 (26.4%) and C_2H_4 (5.3%) at −1.6 V *vs.* RHE. Electrochemical pulsing further increased the electrochemical surface area (∼4.6×) and enhanced carbon-product formation, highlighting the direct link between facet-dependent restructuring, active-site generation, and catalytic performance during eCO_2RR.

Together, these studies demonstrate that the catalyst surface operating during eCO_2RR can differ substantially from the as-prepared state, particularly for polycrystalline or electrodeposited Cu electrodes. EC-AFM reveals that dynamic surface reconstruction, occurring through dissolution–redeposition processes and facet-dependent morphological evolution, continuously modifies the density and coordination of active sites. These structural changes directly influence the adsorption of key intermediates and, consequently, catalytic activity and product selectivity. EC-AFM therefore provides a powerful platform for visualising nanoscale surface dynamics under reaction conditions and highlights the importance of integrating *in situ* microscopy with electrochemical measurements to establish reliable structure–function relationships in eCO_2RR catalysts.

3.2. Electrochemical-scanning tunnelling microscopy (EC-STM)

EC-STM enables atomic-scale visualisation of catalyst surfaces under applied potential, providing unique insight into potential-dependent restructuring and active-site evolution during eCO_2RR. Complementing EC-AFM, EC-STM offers higher spatial resolution and direct access to crystallographic and molecular-scale transformations at electrified interfaces. In particular, EC-STM enables observation of dynamic catalyst transformations that directly influence catalytic activity and selectivity during CO_2 electroreduction.

As an illustrative example of molecular catalyst restructuring, Jeong *et al.* employed *in situ* EC-STM to monitor structural evolution of a Cu-phthalocyanine (CuPc) adlayer on Au(111) during eCO_2RR.[49] STM images revealed that the initially well-ordered CuPc molecular layer rapidly restructured under cathodic bias, forming nanoscale clusters across the surface even at modest reduction potentials (≈ −0.1 V *vs.* Ag/AgCl), with extensive cluster coverage observed at −0.7 V *vs.* Ag/AgCl. These clusters originated from potential-induced demetallation of the CuPc macrocycle, where proton-assisted cleavage of the Cu–N coordination released Cu atoms that subsequently nucleated into Cu-based nanoclusters on the Au surface. *Ex situ* XPS confirmed the decrease of Cu–N bonding and the appearance of N–H species, together with signatures of Cu_xO complexes, indicating that the molecular catalyst transforms into Cu-derived active clusters under reaction conditions. These newly formed Cu_xO nanoclusters act as the operative catalytic sites capable of stabilising key CO intermediates required for CO_2 reduction. Electrochemical characterisation further showed the emergence of a CO_2 reduction peak near −0.7 V *vs.* Ag/AgCl, coinciding with the cluster-covered surface, indicating that the CuPc-derived Cu_xO clusters represent the catalytically active phase. This study demonstrates that molecular $Cu–N_4$ catalysts can dynamically transform into nanoparticulate Cu-based active sites during operation, highlighting how EC-STM directly reveals the structural origin of catalytic activity.

In contrast to CuPc, cobalt phthalocyanine (CoPc) exhibits greater structural stability during eCO_2RR. Wang *et al.* used *in situ* EC-STM to monitor a self-assembled CoPc monolayer on Au(111) and observed two adsorbed species with different contrasts in CO_2-saturated electrolyte (Fig. 7a–d).[50] Approximately 14.2 ± 2.2% of the surface species appeared as high-contrast features in CO_2-saturated electrolyte, whereas their population decreased to 0.70 ± 0.16% in air and 0.19 ± 0.08% in Ar, indicating that the contrast change is directly associated with CO_2 adsorption. These high-contrast species were assigned to a $Co^{(I)}Pc–CO_2$ complex formed after electrochemical reduction of $Co^{(II)}Pc$ to $Co^{(I)}Pc$ near −0.2 V *vs.* SCE, as confirmed by cyclic voltammetry and theoretical simulations. The formation of this $Co^{(I)}Pc–CO_2$ adduct represents the initial CO_2 activation step at the $Co–N_4$ active site, where coordination of CO_2 to the reduced cobalt centre stabilises the adsorbed intermediate required for subsequent reduction to CO. Potential-dependent EC-STM imaging further revealed a reversible transformation between $CoPc–CO_2$ and pristine CoPc during catalytic operation, with the population of the adsorbed intermediate increasing as the potential approaches the $Co^{(II)}/Co^{(I)}$ reduction region. Kinetic analysis based on potential-step EC-STM experiments yielded an apparent rate constant of

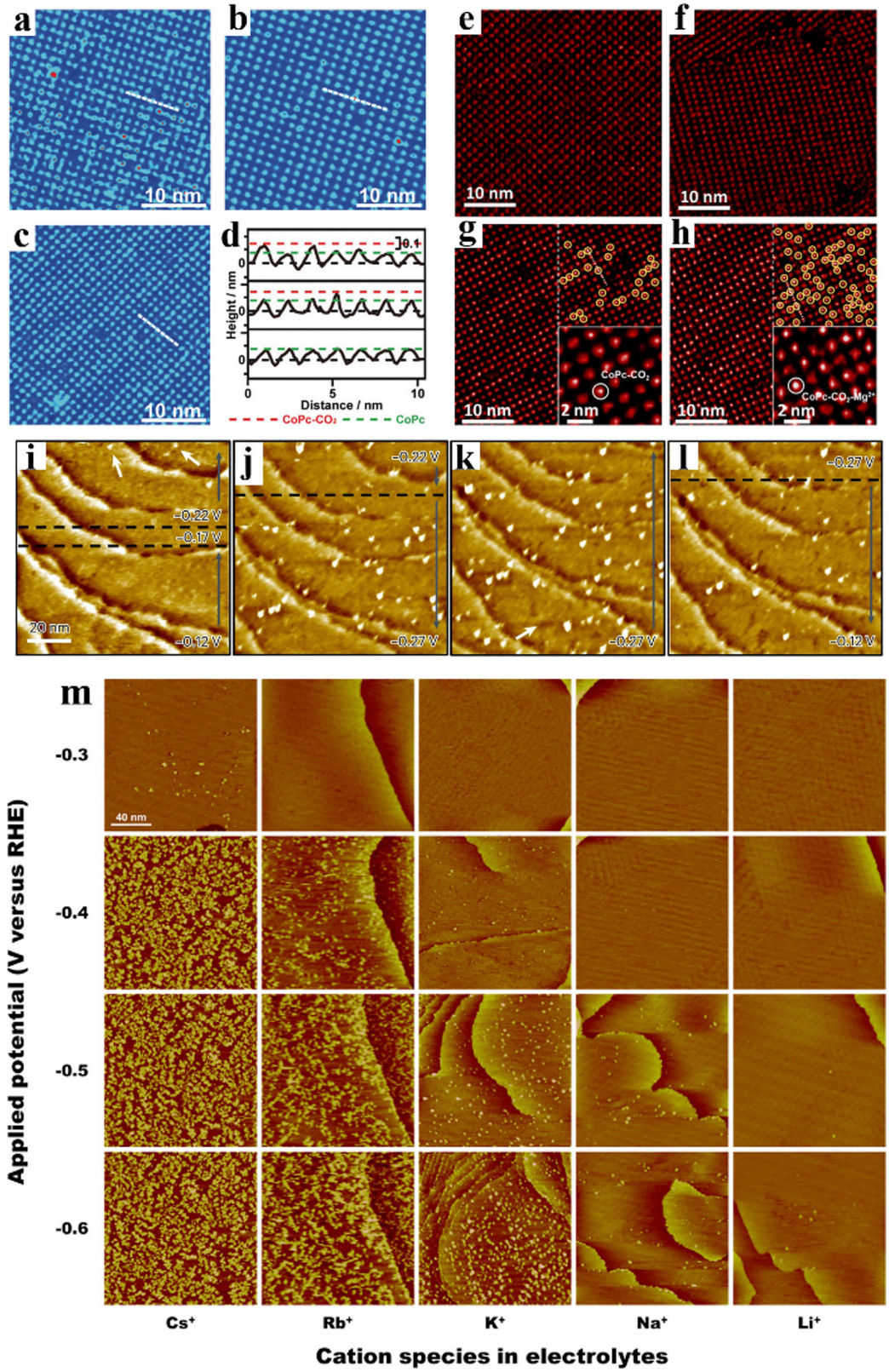

Fig. 7 STM of CoPc monolayer on Au(111) in (a) CO_2, (b) air, (c) Ar, all in 0.1 M $KHCO_3$ and (d) cross-section profile of (a)–(c) from top to bottom. Adapted from ref. 50 with permission from Wiley-VCH GmbH, Copyright 2020. (e)–(h) STM images of CoPc monolayer on Au(111), in Ar (e) and (f), CO_2 (g) and (h), with (e) and (g) in 0.1 M $NaClO_4$ and f and h in 0.1 M $NaClO_4$ with 0.05 M $Mg(ClO_4)_2$, with high-resolution inset images. Adapted from ref. 51 with permission from the American Chemical Society, Copyright 2022. (i)–(l) STM images of Cu(100) with stepwise potential from (i) −0.12 to −0.17 and then to −0.22 (j) decreased to −0.27 V, (k) with potential hold for and (l) change back to −0.12 V. Adapted from ref. 52 under the CC-BY license. (m) STM of potential dependence on surface roughening of Au(111) in CO_2 saturated 0.1 M $LiHCO_3$, $NaHCO_3$, $KHCO_3$, $RbHCO_3$ and $CsHCO_3$ after holding potential for 30 minutes. Adapted from ref. 53 with permission from the American Chemical Society, Copyright 2024.

$\sim 7.9 \times 10^{10}$ molecules cm^{-2} s^{-1} for CO_2 binding to $Co^{(I)}Pc$, confirming that CO_2 coordination to the reduced metal centre is the rate-limiting step governing catalytic turnover. These results provide direct molecular-scale visualisation of intermediate formation during CO_2 reduction and demonstrate how EC-STM can capture adsorbate–catalyst interactions that control activity and selectivity in $Co–N_4$ molecular catalysts.

Beyond identifying catalytic intermediates, EC-STM can also elucidate how electrolyte species modulate catalyst–intermediate interactions. Building on this concept of interfacial modulation, Wang *et al.* used *in situ* EC-STM to investigate the role of Mg^{2+} cations in CoPc-catalysed CO_2 reduction on Au(111).[51] STM imaging (Fig. 7e–h) revealed the formation of high-contrast surface species corresponding to a $CoPc–CO_2–Mg^{2+}$ complex, with apparent molecular heights ($\sim$0.19 nm) larger than those of $CoPc–CO_2$ ($\sim$0.15 nm) and pristine CoPc ($\sim$0.10 nm). The surface coverage of the adsorbed CO_2 complex increased with Mg^{2+} concentration, reaching $\sim 30.8 \pm 2.7\%$ when Mg^{2+} concentration exceeded $\sim$30 mM, compared with $\sim 12.6 \pm 1.9\%$ in Mg^{2+}-free electrolytes. Potential-step EC-STM experiments further showed faster adsorption kinetics in Mg^{2+}-containing electrolytes, yielding CO_2 adsorption and desorption rate constants of k_3 = 0.36 min^{-1} and k_{-3} = 0.89 min^{-1}, compared with k_2 = 0.26 min^{-1} and k_{-2} = 1.77 min^{-1} without Mg^{2+}. Electrocatalysis results showed that CoPc achieves $\sim$80% FE for CO over a broad potential window in Mg^{2+}-containing electrolytes, demonstrating that cation–catalyst interactions enhance CO_2 adsorption and promote efficient CO production.

Similar electrolyte-mediated restructuring phenomena have also been observed for metallic catalysts. Studies by Amirbeigiarab *et al.* on Cu(100) revealed similar restructuring phenomena during CO_2 electroreduction, where *in situ* STM observations showed the formation of Cu nanoclusters that subsequently disperse into adatoms, generating a high density of under-coordinated surface sites (Fig. 7i–l).[52] These dynamically formed sites were correlated with enhanced catalytic activity for CO_2 reduction, promoting C–C coupling pathways and leading to increased selectivity toward multicarbon products such as ethylene and ethanol, with FE approaching $\sim$40–50% for C_{2+} products at current densities on the order of tens of mA cm^{-2} under eCO_2RR conditions. The emergence of these active configurations near the onset of CO_2 reduction highlights the intrinsic structural flexibility of Cu surfaces under cathodic potentials. Taken together, these results suggest that electrolyte cations can actively influence restructuring processes, potentially through modulation of the interfacial electric field, specific adsorption at the catalyst surface, or stabilisation of transient hydride-like intermediates that facilitate surface atom mobility and the generation of catalytically active low-coordination sites.

The influence of electrolyte cations extends even further, affecting surface reconstruction on noble metal catalysts as well. Using a model Au(111) single crystal, Wang *et al.* systematically examined the effects of alkali metal cations (Cs^+, Rb^+, K^+, Na^+, Li^+) under identical bicarbonate conditions (Fig. 7m).[53] Their *in situ* electrochemical STM measurements revealed pronounced cation-dependent surface restructuring, with the extent of Au surface roughening following the trend Cs^+ (37.1%) > Rb^+ (25.7%) > K^+ (16.6%) > Na^+ (2.3%) > Li^+ (0.3%). The roughened surfaces contain a high density of low-coordinated Au atoms, which serve as highly active catalytic sites for CO_2 electroreduction. Correspondingly, catalytic measurements demonstrated that electrolytes containing larger alkali cations exhibited significantly enhanced activity and selectivity toward CO formation, with increased FE and higher partial current densities compared with smaller cations such as Li^+. This strong correlation between cation size, surface restructuring, and catalytic performance highlights the crucial role of electrolyte composition in dynamically generating active sites during operation. These findings suggest that weakly hydrated, large alkali cations promote interfacial electric-field amplification and stabilise surface intermediates, thereby facilitating surface atom mobility and the formation of catalytically active low-coordination metal sites.

Collectively, EC-STM studies demonstrate that catalyst surfaces, whether molecular or metallic, are highly dynamic under eCO_2RR conditions. Potential-driven restructuring, metal demetallation, intermediate stabilisation, and electrolyte-induced morphology changes all contribute to the evolving active phase. By directly visualising these transformations at atomic and molecular scales, EC-STM provides critical insight into the structure–activity relationships governing CO_2 electroreduction. These insights highlight the necessity of *in situ* atomic-scale imaging to accurately identify active species and establish reliable structure–activity relationships in CO_2 electroreduction.

3.3. Electrochemical-transmission electron microscopy (EC-TEM)

EC-TEM extends nanoscale characterisation into realistic reaction environments by integrating liquid electrochemical cells within the TEM column. These specialised microfabricated cells contain a CO_2-saturated electrolyte and patterned electrodes, enabling real-time imaging of structural evolution under applied bias. Beyond morphological changes, EC-TEM can provide insight into crystalline phase transitions, lattice dynamics, defect formation, and particle reshaping during operation, thereby enabling direct visualisation of catalyst restructuring under working electrochemical conditions. Such capability makes EC-TEM a uniquely powerful technique for correlating nanoscale structural dynamics with catalytic behaviour in eCO_2RR systems.

Zhang *et al.* employed EC-TEM to investigate Cu nanowires under eCO_2RR conditions and observed striking dynamic restructuring behaviour.[54] Real-time imaging under cathodic bias (−1.1 V *vs.* RHE) allowed direct visualisation of structural fluctuations at the nanoscale, revealing that initially well-ordered crystalline Cu nanowires undergo rapid and reversible structural transformations during electrochemical operation (Fig. 8a–c). Upon application of cathodic bias, initially crystalline Cu regions underwent localised amorphisation. These

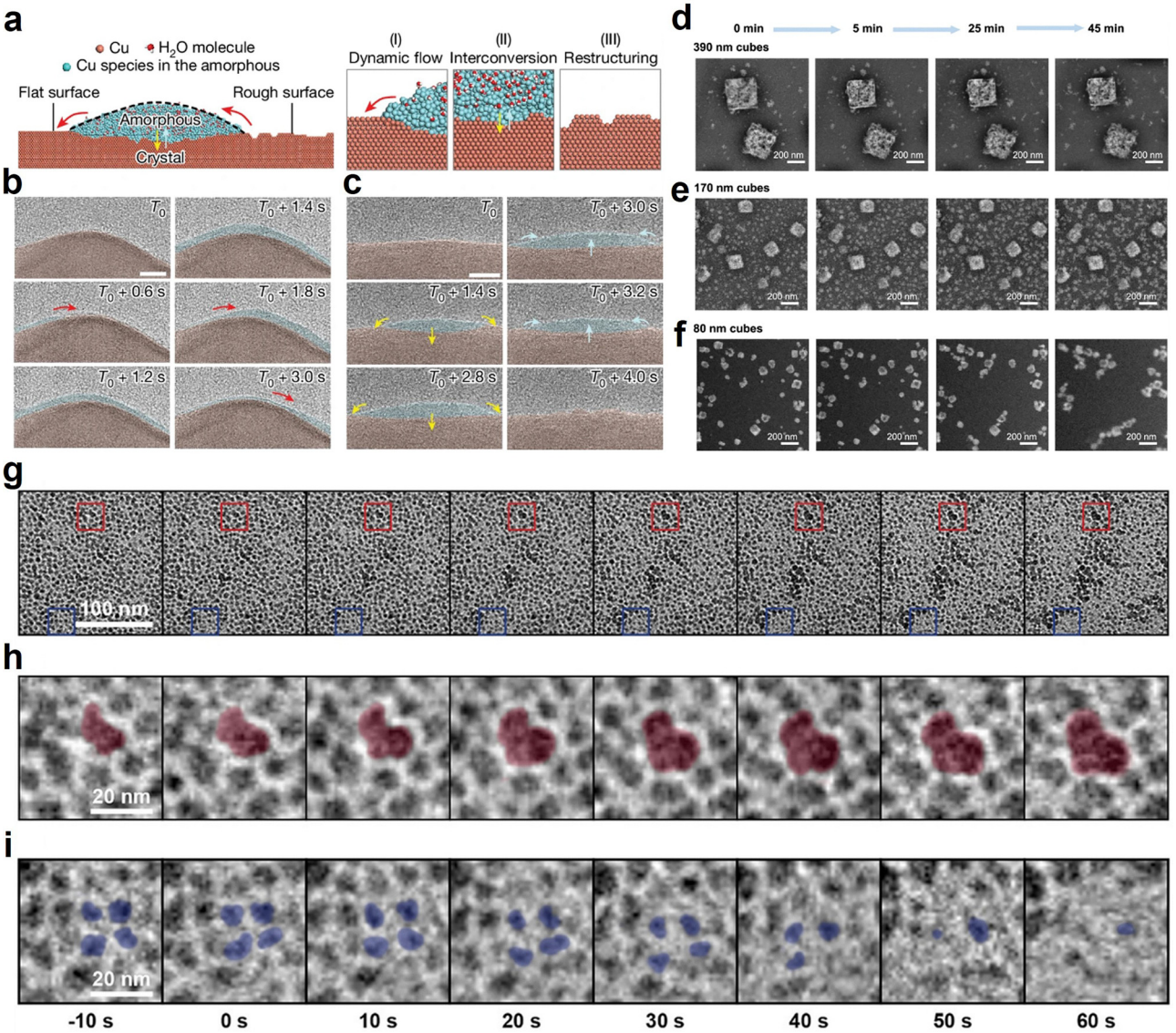

Fig. 8 (a) The schematic shows that the amorphous interphase mediates the crystalline Cu surface restructuring through dynamic flow and interconversion behaviours, (b) HRTEM images show the liquid-like flow of the amorphous on the crystalline Cu surface, (c) HRTEM images show the interconversion between crystalline Cu and amorphous interphase. Scale bar, 5 nm for both (b) and (c). Adapted from ref. 54 with permission from Springer Nature, Copyright 2024. Snapshots extracted from the videos tracking the evolution of (d) 390 nm, (e) 170 nm, and (f) 80 nm Cu cubes at 0, 5, 25, and 45 minutes after applying a potential of −0.9 V *vs.* RHE. Adapted from ref. 55 under the CC-BY license. (g) Sequence of TEM images taken while applying −0.25 V *vs.* RHE, (h) magnified images of red frame depicting the secondary particle growth process at higher magnification, (i) magnified images of blue frame depicting the shrinking process of the primary particles. Adapted from ref. 56 with permission from Wiley-VCH GmbH, Copyright 2020.

amorphous domains were highly transient and spatially confined, exhibiting pulsating transitions between crystalline and disordered states over short timescales. Electron energy loss spectroscopy (EELS) revealed that the amorphous regions consisted of mixed-valence $Cu^{(0)}/Cu^{(I)}$ species, indicating partial oxidation–reduction cycling of Cu atoms at the catalyst surface. Moreover, individual Cu atoms were extracted from the lattice, generating atomic vacancies that were rapidly refilled, preserving overall crystallinity but leaving persistent defects, particularly at step edges. These defects evolved into nanoscale pits over time, increasing surface roughness and the density of catalytically accessible active sites. The formation of these defect-rich regions and under-coordinated Cu atoms is particularly significant because such sites are widely recognised as highly active sites for CO_2 reduction and C–C coupling reactions, which are commonly associated with enhanced activity and selectivity toward multicarbon products in Cu-based catalysts.

Size-dependent restructuring effects were further demonstrated by Grosse *et al.*, who examined Cu_2O nanocubes of varying dimensions. Real-time imaging revealed pronounced size-dependent structural evolution of the nanocubes under

cathodic bias, with the smallest cubes (80 nm) exhibiting the most significant transformation (Fig. 8d–f).[55] These nanoparticles underwent continuous Cu atom detachment, dissolution, and subsequent redeposition processes, resulting in substantial morphological rearrangement of the catalyst surface.

During eCO_2RR, 80 nm cubes increased in size due to redeposited Cu, while their population decreased by ~50% within 1 hour. This loss was attributed to weaker adhesion to the support and higher surface mobility of the small nanoparticle, which facilitated migration and coalescence during electrochemical operation. In contrast, larger cubes (170 and 390 nm) displayed significantly greater structural stability, maintaining relatively constant size and morphology throughout the experiment. These results highlight the strong influence of nanoparticle size and catalyst–support interactions on restructuring dynamics and durability during electrochemical CO_2 reduction, emphasising that nanoscale catalysts can undergo extensive restructuring that fundamentally alters active-site distribution and surface chemistry during operation.

Complementary *in situ* TEM studies by Vavra *et al.* further confirmed Cu dissolution at OCP, followed by redeposition under CO_2RR bias (Fig. 8g–i).[56] Real-time imaging revealed that Cu atoms dissolve from the catalyst surface even before electrochemical reduction begins, and subsequently redeposit as isolated single atoms or small clusters once a cathodic potential is applied. The redeposited Cu formed isolated single atoms or small clusters, generating active-site configurations different from the as-prepared catalyst. Such dynamically generated atomic Cu species and nanoscale clusters can significantly modify the distribution of catalytic active sites during operation. Although this study primarily focused on *in situ* structural evolution and did not report detailed catalytic performance metrics such as FE, product selectivity, or current density, the observations provide important mechanistic insight into how dissolution–redeposition processes can generate highly dispersed Cu sites that are widely considered active for CO_2 reduction. These findings further demonstrate that catalyst restructuring may occur before steady-state catalysis begins, complicating the interpretation of *ex situ* characterisation and reinforcing conclusions drawn from EC-AFM and EC-STM regarding Cu instability under electrochemical conditions.

While Cu systems highlight dynamic restructuring, studies on alternative catalysts underscore the importance of intrinsic stability. Abdellah *et al.* investigated palladium (Pd) electrodes for CO_2RR and observed no morphological changes under OCP, indicating that Pd nanoparticles remain structurally stable in the absence of electrochemical bias.[57] However, upon applying −0.2 V *vs.* RHE, rapid particle migration, agglomeration, and detachment occurred within seconds. The Pd particles evolved into hollow, sponge-like structures, attributed to the rapid formation of Pd hydride phases. Hydride formation-induced mechanical stress within the particles drives deformation and detachment. The insertion of hydrogen into the Pd lattice leads to significant lattice expansion, generating internal strain that promotes particle restructuring and morphological instability. This hydride-induced structural transformation highlights how reactive intermediates formed during electrochemical reactions can dramatically alter catalyst morphology and stability, demonstrating that even catalysts that appear structurally stable at open-circuit conditions may undergo rapid restructuring once electrochemical reactions generate reactive species such as metal hydrides.

Overall, EC-TEM studies demonstrate that catalyst morphology, phase composition, and defect structure are highly dynamic during eCO_2RR. Dissolution–redeposition processes, amorphisation, vacancy formation, particle migration, and hydride-induced deformation all contribute to the evolution of active-site landscapes. These *in situ* observations emphasise that the true catalytic surface often differs significantly from the as-synthesised material, underscoring that catalyst stability, both under OCP and operating bias, must be considered a primary design criterion alongside activity and selectivity. Integrating electron microscopy with complementary spectroscopic techniques is therefore essential for constructing accurate structure–function relationships and guiding the development of robust next-generation eCO_2RR catalysts. A summary of representative *in situ* microscopic studies that visualise catalyst restructuring during eCO_2RR is provided in Table 4.

In summary, *in situ*/*operando* spectroscopy and microscopy establish a direct bridge between descriptor energetics, surface dynamics, and product selectivity, forming the foundation for mechanistically guided catalyst design. By revealing how catalyst structures dynamically evolve under working conditions, these techniques enable the identification of true active phases and provide critical insights for the rational development of stable and selective CO_2 reduction catalysts.

In addition to the spectroscopy and microscopy techniques discussed here, complementary methods such as differential electrochemical mass spectrometry (DEMS),[58,59] *in situ*/*operando* X-ray diffraction (XRD)[60,61] provide additional insights into eCO_2RR. DEMS enables real-time detection of volatile reaction products and, in some cases, can approach *operando* conditions when directly correlated with electrochemical measurements, while XRD reveals bulk phase transformations of catalysts under working conditions. Although these techniques are not the primary focus of this review, they play an important role in developing a comprehensive understanding of CO_2 reduction mechanisms. A comparison of the capabilities and limitations of commonly used *in situ*/*operando* techniques is summarised in Table 5. These inherent trade-offs in sensitivity and resolution underpin many of the challenges in identifying active sites and reaction mechanisms, as discussed in the following section.

4. Challenges in identifying active sites and reaction mechanisms in eCO_2RR

Despite significant advances in *operando* characterisation, identifying the true catalytically active phase in eCO_2RR

Table 4 Summary of *in situ* microscopy studies revealing catalyst restructuring during eCO_2RR

Technique	Ref.	Catalyst system	Analysis insight	Intermediate	Catalytic implication
EC-AFM	Simon *et al.*[47]	Cu(100) single-crystal	Potential-dependent surface reconstruction forms under-coordinated Cu sites	*CO	Defect-sites enhance C_{2+} products
EC-AFM	Wang *et al.*[48]	Polycrystalline Cu	Alternating anodic and cathodic pulses generate low-coordination Cu sites, facilitating C–C coupling	*CO	CO/formate at low bias and C_2 products at high bias
EC-STM	Jeong *et al.*[49]	CuPc/Au(111)	Molecular Cu-N4 catalyst dynamically transforms into catalytically active Cu_xO nanoclusters	*CO	Cu_xO nanoclusters active for eCO_2RR
EC-STM	Wang *et al.*[50]	CoPc/Au(111)	Potential-dependent CoPc–CO_2 complex formation represents activation of CO_2	Co(I)Pc–CO_2 complex	CO formation
EC-STM	Wang *et al.*[51]	CoPc/Au(111) + Mg^{2+} electrolyte	Mg^{2+} stabilises the adsorbed CO_2 complex, promoting selective CO formation	CoPc–CO_2–Mg^{2+} complex	CO (80% FE)
EC-STM	Amirbeigiarab *et al.*[52]	Cu(100) single crystal	CO-induced Cu adatoms and nanoclusters create undercoordinated Cu sites	*CO, *COOH	C_{2+} formation
EC-STM	Wang *et al.*[53]	Au(111) single crystal	Large cation-induced Au nanoclusters (1–3 nm) form catalytically active low-coordinated Au atoms	*CO	Enhanced CO selectivity
EC-TEM	Zhang *et al.*[54]	Cu nanowires	Dynamic Cu reconstruction under bias generates defect-rich regions and low-coordination Cu sites	*CO	Promotes C–C coupling
EC-TEM	Grosse *et al.*[55]	Cu_2O nanocubes (80–390 nm)	Small cubes undergo dissolution and redeposition, migration, and coalescence, while large cubes do not change	*CO	High C_{2+} selectivity
EC-TEM	Vavra *et al.*[56]	~7 nm Cu nanoparticles	Dissolution-reposition forms single atoms and nanocluster active sites	Cu^+/Cu^{2+} (catalyst state)	C–C coupling enhancement
EC-TEM	Abdellah *et al.*[57]	Pd nanoparticles	Pd → PdH_x lattice expansion is catalytically active	*H, *OCHO	Formate production

Note: In microscopy studies, intermediates (*e.g.*, *CO, *COOH) are typically inferred from structural evolution and reaction conditions, rather than directly observed, unless explicitly identified at the molecular level.

remains a fundamental challenge. Catalysts often undergo substantial structural and electronic transformations under reaction conditions, meaning that the active phase may differ significantly from the as-prepared material. While *in situ* and *operando* techniques provide direct insight into catalyst behaviour, their reliability depends on spatial and temporal resolution, sensitivity to surface species, and the ability to correlate observations with catalytic performance. A key limitation of current *in situ* techniques lies in their ability to detect highly transient intermediates. Vibrational spectroscopies such as SERS and ATR-FTIR are highly effective for identifying relatively stable, surface-bound species, but may not capture short-lived intermediates with low surface coverage. Similarly, XAS provides robust information on oxidation states and coordination environments, yet is limited in its ability to resolve ultrafast dynamic processes. As a result, some mechanistic steps may be inferred rather than directly observed.

In addition to instrumental limitations, uncertainties also arise in the interpretation of *in situ* experimental data. Spectroscopic signatures of reaction intermediates can sometimes overlap, making accurate assignment challenging, particularly for complex reaction networks such as eCO_2RR. Low signal-to-noise ratios and limited surface sensitivity may further obscure detection of low-coverage species. Moreover, dynamic catalyst restructuring under reaction conditions can lead to the coexistence of multiple active states, complicating the identification of the dominant catalytic phase. Consequently, mechanistic conclusions drawn from a single technique may be uncertain.

These challenges contribute to differing and sometimes conflicting mechanistic interpretations reported in the literature. For example, in Cu-based systems, some studies attribute enhanced C–C coupling to increased *CO surface coverage,[4,62] while others emphasise the role of Cu^+/Cu^0 interfaces in stabilising *CO–CO intermediates.[63,64] Similarly, for formate-selective catalysts such as Sn- and Bi-based materials, both *COOH[37,44] and *OCHO[39,45] pathways have been proposed depending on catalyst structure and reaction conditions. Such discrepancies often arise from differences in catalyst morphology, electrolyte composition, applied potential, and the inherent constraints of individual characterisation techniques.

Resolving these discrepancies requires a correlative approach that integrates multiple *in situ* techniques with catalytic performance metrics. By combining spectroscopic identification of reaction intermediates, structural insights into catalyst material from microscopy, and electrochemical measurements, it becomes possible to distinguish transient species from catalytically relevant active states. This integrated strategy is essential for establishing reliable structure–activity relationships and developing a unified mechanistic understanding of eCO_2RR. Continued advances in time-resolved and multimodal *operando* techniques are expected to further improve the detection of short-lived intermediates and enable more definitive identification of active phases under realistic reaction conditions.

Despite these challenges, several representative studies demonstrate how *operando* characterisation can successfully establish structure–activity relationships and guide catalyst design. For example, XAS investigations of Cu-based catalysts have revealed the formation of mixed Cu^+/Cu^0 interfacial sites under reaction conditions, which stabilise *CO–CO intermediates and promote C–C coupling.[42] These insights have guided the development of oxide-derived Cu catalysts with enhanced selectivity toward C_{2+} products. Similarly, spectroscopic studies on Bi-based catalysts have identified the stabilisation of *OCHO

Table 5 Comparison of strengths and limitations of various *in situ*/*operando* techniques for studying eCO_2RR

Technique	Sensitivity to reaction intermediates	Spatial resolution	Temporal resolution	Key strengths	Key limitations
SERS	High (surface species)	Nanoscale (~10–100 nm, hotspot-dependent)	ms–s	Detects adsorbed intermediates (*CO, *OCHO *COOH)	Signal depends on substrate; limited quantification
ATR-FTIR/SEIRAS	High (vibrational modes)	Surface-sensitive (evanescent probing depth ~100 nm)	s–min	Identifies functional groups and reaction pathways of surface intermediates	Overlapping bands; limited sensitivity to low coverage
XAS/XAFS	Moderate (electronic structure)	No spatial resolution (ensemble-averaged signal)	s–min	Reveals oxidation states and the coordination environment of the catalyst	Limited surface specificity; lower temporal resolution
EC-STM/EC-AFM	Low (no direct detection of reaction intermediates)	Atomic–nanoscale (~0.1–10 nm)	s–min	Reveals real-space surface structure and reconstruction of the catalyst	Cannot directly detect reaction intermediates; relatively slow imaging
EC-TEM	Low (no direct detection of reaction intermediates)	Atomic scale	ms–s	Direct visualisation of the dynamic restructuring of the catalyst	Beam effects; complex experimental environment
DEMS	None (no direct detection of reaction intermediates)	None (bulk detection)	ms–s	Detects real-time reaction products	Limited to gaseous products; no structural info on the catalyst
XRD	Low (catalyst phase only)	Bulk	s–min	Identifies phase transitions in the catalyst	No catalyst surface or reaction intermediate information

intermediates as a key determinant of formate selectivity.[45] In contrast, XAS studies on Sn-based catalysts have highlighted the importance of mixed Sn^{2+}/Sn^0 oxidation states in promoting the formate pathway.[44] These findings demonstrate that different catalyst systems can favour distinct mechanistic pathways toward formate production. In these examples, integrating *operando* insights with catalyst design can bridge the gap between mechanistic understanding and practical catalyst development in eCO_2RR systems.

5. Future directions in *in situ*/*operando* eCO_2RR characterisation

Understanding the complex mechanisms of electrochemical CO_2 reduction requires characterisation techniques capable of probing catalysts under realistic operating conditions. *In situ* and *operando* characterisation methods have therefore become indispensable tools for revealing the dynamic behaviour of catalysts during CO_2 electroreduction. These techniques enable direct observation of intermediate formation, catalyst restructuring, and active-site evolution, providing critical insight into the mechanisms governing catalytic activity and selectivity. By capturing the catalyst surface under working electrochemical conditions, *in situ* methods are increasingly redefining our understanding of the true catalytically active phase in CO_2 reduction systems.

Despite significant progress, several challenges remain in fully capturing the complexity of catalytic processes under electrochemical conditions. Many current techniques still face limitations in spatial resolution, temporal resolution, and sensitivity to transient reaction intermediates. Future advances in instrumentation and experimental design will therefore be essential for achieving a more comprehensive understanding of CO_2 reduction mechanisms. In particular, improving the ability to detect low-concentration intermediates and track atomic-scale restructuring under realistic electrochemical environments will be critical for establishing reliable structure–activity relationships.

One important direction is the development of multimodal *operando* platforms that combine complementary spectroscopic and microscopic techniques. For example, integrating spectroscopy with high-resolution microscopy could simultaneously reveal chemical intermediate formation and structural evolution of catalysts during reaction. Such correlative approaches will enable direct linking of reaction intermediates with dynamic changes in catalyst morphology and active-site configuration. The integration of these complementary techniques will allow researchers to bridge the gap between molecular-scale reaction chemistry and nanoscale catalyst restructuring.

Another emerging opportunity lies in improving temporal resolution to capture short-lived intermediates and rapid catalyst restructuring events that occur during electrochemical operation. Advances in fast spectroscopy, time-resolved microscopy, and advanced detector technologies will allow

researchers to observe catalytic processes on relevant timescales and provide deeper insight into reaction kinetics and dynamic catalyst evolution. These developments will help reveal transient catalytic states that often remain hidden in conventional steady-state measurements.

In addition, future *operando* studies should increasingly focus on realistic reaction environments, including higher current densities, industrially relevant electrolytes, and gas-diffusion electrode architectures. Such conditions are critical for bridging the gap between fundamental laboratory studies and practical electrochemical CO_2 conversion technologies. The integration of advanced data analysis approaches, including machine learning and automated image analysis, also presents new opportunities for extracting mechanistic insights from large *operando* datasets. These tools can help identify correlations between catalyst structure, intermediate formation, and product selectivity that may not be immediately apparent through conventional analysis methods. Combining *in situ* measurements with data-driven analysis may therefore accelerate the discovery of new catalyst design principles for efficient CO_2 conversion.

Overall, continued development and integration of *in situ*/*operando* spectroscopy and microscopy techniques will be essential for uncovering the true catalytically active phases and dynamic restructuring processes that govern CO_2 electroreduction. Such insights will ultimately guide the rational design of next-generation catalysts with improved activity, selectivity, and stability for sustainable carbon conversion technologies. As these methodologies continue to evolve, *operando* characterisation is expected to play an increasingly central role in bridging fundamental electrochemical science with scalable carbon utilisation technologies.

Looking forward, several emerging directions are expected to further advance *in situ* studies in eCO_2RR. One important development is the integration of hyphenated techniques, where complementary spectroscopy and microscopy methods are combined within a single electrochemical cell to simultaneously probe intermediates, electronic structure, and morphological evolution. Such multimodal approaches enable direct correlation of chemical and structural dynamics under identical reaction conditions. In parallel, the increasing complexity and volume of experimental datasets are driving the adoption of machine learning and data-driven analysis tools to extract meaningful correlations between catalyst structure, intermediate formation, and catalytic performance. These approaches offer new opportunities for identifying hidden patterns and accelerating catalyst discovery. Furthermore, advances in high-speed and fast-scanning probe techniques, such as high-speed AFM, are enabling the capture of dynamic surface processes with improved temporal resolution, providing new insight into rapid restructuring events that occur during electrochemical reactions. Recent developments in this area highlight the potential of such approaches to resolve transient states of the catalyst under realistic conditions.[30] Together, these emerging strategies are expected to enable a more comprehensive, spatially- and time-resolved understanding of catalyst behaviour, ultimately bridging the gap between fundamental mechanistic studies and practical catalyst design.

Conflicts of interest

There are no conflicts to declare.

Data availability

This article reviews previously published literature and does not report new experimental or computational data. All information supporting the conclusions of this work is available in the cited references.

Acknowledgements

The authors acknowledge the financial support from the Engineering and Physical Sciences Research Council (EPSRC), project Metal Atoms on Surfaces and Interfaces (MASI) for Sustainable Future (EP/V000055/1) and EPSRC/SFI CDT in Sustainable Chemistry – Atoms 2 Products (EP/S022236/1).

References

1 Intergovernmental Panel on Climate Change (IPCC), *AR6 Synthesis Report*, 2023.
2 C. Hepburn, E. Adlen, J. Beddington, E. A. Carter, S. Fuss, N. Mac Dowell, J. C. Minx, P. Smith and C. K. Williams, *Nature*, 2019, **575**, 87–97.
3 J. Artz, T. E. Müller, K. Thenert, J. Kleinekorte, R. Meys, A. Sternberg, A. Bardow and W. Leitner, *Chem. Rev.*, 2018, **118**, 434–504.
4 S. Nitopi, E. Bertheussen, S. B. Scott, X. Liu, A. K. Engstfeld, S. Horch, B. Seger, I. E. L. Stephens, K. Chan, C. Hahn, J. K. Nørskov, T. F. Jaramillo and I. Chorkendorff, *Chem. Rev.*, 2019, **119**, 7610–7672.
5 Y. Y. Birdja, E. Pérez-Gallent, M. C. Figueiredo, A. J. Göttle, F. Calle-Vallejo and M. T. M. Koper, *Nat. Energy*, 2019, **4**, 732–745.
6 A. A. Gokhale, J. A. Dumesic and M. Mavrikakis, *J. Am. Chem. Soc.*, 2008, **130**, 1402–1414.
7 W. Li, J. Gan, Y. Liu, Y. Zou, S. Zhang and Y. Qu, *Angew. Chem., Int. Ed.*, 2023, **62**, e202305661.
8 N. Luo, W. Yang, L. Feng, S. Huang, P. Huang and M. Wei, *Mol. Catal.*, 2024, **553**, 113683.
9 W. Wu, J. Luo, J. Zhao, M. Wang, L. Luo, S. Hu, B. He, C. Ma, H. Li and J. Zeng, *Nat. Commun.*, 2024, **15**, 6108.
10 T. Hisatomi and K. Domen, *Nat. Catal.*, 2019, **2**, 387–399.
11 Q. Wang and K. Domen, *Chem. Rev.*, 2020, **120**, 919–985.
12 P. De Luna, C. Hahn, D. Higgins, S. A. Jaffer, T. F. Jaramillo and E. H. Sargent, *Science*, 2019, **364**, eaav3506.
13 T. Chen, Z. Zhao, S. Zhang, B. Ding, D. Chen, G. Chen, Y. Zhu and X. Zhang, *Adv. Energy Mater.*, 2025, **15**, 2502092.
14 X. Ke, W. Xu, C. Liu, Y. Wang, X. Huang, R. Xiao, X. Xu, T. Li and Z. Shao, *Energy Environ. Sci.*, 2025, **18**, 7792–7858.
15 H.-R. Molly Jhong, S. Ma and P. J. A. Kenis, *Curr. Opin. Chem. Eng.*, 2013, **2**, 191–199.
16 E. E. Benson, C. P. Kubiak, A. J. Sathrum and J. M. Smieja, *Chem. Soc. Rev.*, 2009, **38**, 89–99.
17 T. Tang, X. Bai, Z. Wang and J. Guan, *Chem. Sci.*, 2024, **15**, 5082–5112.
18 S. Sahoo, K. Y. Wickramathilaka, E. Njeri, D. Silva and S. L. Suib, *Front. Chem.*, 2024, **12**, 1374878.
19 L. Liu and A. Corma, *Chem. Rev.*, 2023, **123**, 4855–4933.
20 J. S. Bates, *Nat. Chem.*, 2025, **17**, 318–324.
21 S. Mitchell, R. Qin, N. Zheng and J. Pérez-Ramírez, *Nat. Nanotechnol.*, 2021, **16**, 129–139.

22 J. T. Feaster, C. Shi, E. R. Cave, T. Hatsukade, D. N. Abram, K. P. Kuhl, C. Hahn, J. K. Nørskov and T. F. Jaramillo, *ACS Catal.*, 2017, **7**, 4822–4827.
23 T. Burwell, M. Thangamuthu, G. N. Aliev, S. Ghaderzadeh, E. C. Kohlrausch, Y. Chen, W. Theis, L. T. Norman, J. A. Fernandes, E. Besley, P. Licence and A. N. Khlobystov, *Commun. Chem.*, 2024, **7**, 140.
24 T. Burwell, M. Thangamuthu, E. Besley, Y. Chen, J. Pyer, J. Alves Fernandes, A. E. Lanterna, P. Licence, G. N. Aliev, W. Theis and A. N. Khlobystov, *ACS Appl. Energy Mater.*, 2025, **8**, 2281–2290.
25 X. Wang, W. Ju, L. Liang, M. Riyaz, A. Bagger, M. Filippi, J. Rossmeisl and P. Strasser, *Angew. Chem., Int. Ed.*, 2024, **63**, e202401821.
26 F. Dattila, R. R. Seemakurthi, Y. Zhou and N. López, *Chem. Rev.*, 2022, **122**, 11085–11130.
27 Y. Xue, M. He, P. Wang, C. Yang, J. Yao, T. Zhang, H. Xu, X. Sun and Z. Li, *J. Phys. Chem. C*, 2024, **128**, 19109–19121.
28 B. Hasa, Y. Zhao and F. Jiao, *Annu. Rev. Chem. Biomol. Eng.*, 2023, **18**, 165–185.
29 M. A. Bañares and M. Daturi, *Catal. Today*, 2023, **423**, 114255.
30 R. Sun, X. Liu, J. Huang, Y. Wang, H. Huang, Y. Lei and J. Ge, *Small Methods*, 2025, **9**, 2500516.
31 M. Zhang, Z. Chen and Y. A. Wu, *Adv. Funct. Mater.*, 2026, **36**, e29196.
32 I. V. Chernyshova, P. Somasundaran and S. Ponnurangam, *Proc. Natl. Acad. Sci. U. S. A*, 2018, **115**, E9261–E9270.
33 C. Zhan, F. Dattila, C. Rettenmaier, A. Bergmann, S. Kühl, R. García-Muelas, N. López and B. R. Cuenya, *ACS Catal.*, 2021, **11**, 7694–7701.
34 D. Chen, Y. Wei, Z. Sun, X. Zhao, X. Tang, X. Zhu, G. Li, L. Yao, S. Chen, R. Lin, J. Wang, Q. Li, X. Fan, T. Qiu and Q. Hao, *Small*, 2025, **21**, 2409569.
35 J. Gao, H. Zhang, X. Guo, J. Luo, S. M. Zakeeruddin, D. Ren and M. Grätzel, *J. Am. Chem. Soc.*, 2019, **141**, 18704–18714.
36 Y. Wang, J. Wang, R. Cai, J. Zhang, S. Xia, Z. Li, C. Yu, J. Wu, P. Wang and Y. Wu, *Adv. Funct. Mater.*, 2025, **35**, 2417764.
37 W. Liu, Y. Wen, N. Fang, M. Wang, Y. Xu and X. Huang, *Chem. Commun.*, 2023, **59**, 11843–11846.
38 E. P. Delmo, Y. Wang, Y. Song, S. Zhu, H. Zhang, H. Xu, T. Li, J. Jang, Y. Kwon, Y. Wang and M. Shao, *J. Am. Chem. Soc.*, 2024, **146**, 1935–1945.
39 X.-D. Liang, Q.-Z. Zheng, N. Wei, Y.-Y. Lou, S.-N. Hu, K.-M. Zhao, H.-G. Liao, N. Tian, Z.-Y. Zhou and S.-G. Sun, *Nano Energy*, 2023, **114**, 108638.
40 K. S. Adarsh, N. Chandrasekaran and V. Chakrapani, *Front. Chem.*, 2020, **20**, 137.
41 B. Chang, H. Pang, F. Raziq, S. Wang, K.-W. Huang, J. Ye and H. Zhang, *Energy Environ. Sci.*, 2023, **16**, 4714–4758.
42 S.-C. Lin, C.-C. Chang, S.-Y. Chiu, H.-T. Pai, T.-Y. Liao, C.-S. Hsu, W.-H. Chiang, M.-K. Tsai and H. M. Chen, *Nat. Commun.*, 2020, **11**, 3525.
43 J. Feijóo, Y. Yang, M. V. Fonseca Guzman, A. Vargas, C. Chen, C. J. Pollock and P. Yang, *J. Am. Chem. Soc.*, 2023, **145**, 20208–20213.
44 A. Dutta, A. Kuzume, V. Kaliginedi, M. Rahaman, I. Sinev, M. Ahmadi, B. Roldán Cuenya, S. Vesztergom and P. Broekmann, *Nano Energy*, 2018, **53**, 828–840.
45 S. Zhao, H. Zhou, D. Cao, B. Sheng, F. Qian, C. Liu, Y. Chu, R. Li, L. Song and S. Chen, *Chem. Res. Chin. Univ.*, 2025, **41**, 273–280.
46 A. Martini, J. Timoshenko, M. Rüscher, D. Hursán, M. C. O. Monteiro, E. Liberra and B. R. Cuenya, *J. Synchrotron Radiat.*, 2024, **31**, 741–750.
47 G. H. Simon, C. S. Kley and B. Roldan Cuenya, *Angew. Chem., Int. Ed.*, 2021, **60**, 2561–2568.
48 H. Wang, L. D. B. Mandemaker, J. de Ruiter, X. Yu, W. van der Stam and B. M. Weckhuysen, *Angew. Chem., Int. Ed.*, 2025, **64**, e202424530.
49 Y. Jeong, Y. Kim, Y. J. Kim and J. Y. Park, *Adv. Sci.*, 2024, **11**, 2304735.
50 X. Wang, Z.-F. Cai, Y.-Q. Wang, Y.-C. Feng, H.-J. Yan, D. Wang and L.-J. Wan, *Angew. Chem., Int. Ed.*, 2020, **59**, 16098–16103.
51 Y.-Q. Wang, X.-H. Dan, X. Wang, Z.-Y. Yi, J. Fu, Y.-C. Feng, J.-S. Hu, D. Wang and L.-J. Wan, *J. Am. Chem. Soc.*, 2022, **144**, 20126–20133.
52 R. Amirbeigiarab, J. Tian, A. Herzog, C. Qiu, A. Bergmann, B. Roldan Cuenya and O. M. Magnussen, *Nat. Catal.*, 2023, **6**, 837–846.
53 Y.-Q. Wang, J. Fu, Y. Feng, K. Zhao, L. Wang, J.-Y. Cai, X. Wang, T. Chen, F. Yang, J.-S. Hu, B. Xu, D. Wang and L.-J. Wan, *J. Am. Chem. Soc.*, 2024, **146**, 27713–27724.
54 Q. Zhang, Z. Song, X. Sun, Y. Liu, J. Wan, S. B. Betzler, Q. Zheng, J. Shangguan, K. C. Bustillo, P. Ercius, P. Narang, Y. Huang and H. Zheng, *Nature*, 2024, **630**, 643–647.
55 P. Grosse, A. Yoon, C. Rettenmaier, A. Herzog, S. W. Chee and B. Roldan Cuenya, *Nat. Commun.*, 2021, **12**, 6736.
56 J. Vavra, T.-H. Shen, D. Stoian, V. Tileli and R. Buonsanti, *Angew. Chem., Int. Ed.*, 2021, **60**, 1347–1354.
57 A. M. Abdellah, F. Ismail, O. W. Siig, J. Yang, C. M. Andrei, L.-A. DiCecco, A. Rakhsha, K. E. Salem, K. Grandfield, N. Bassim, R. Black, G. Kastlunger, L. Soleymani and D. Higgins, *Nat. Commun.*, 2024, **15**, 938.
58 D. van den Berg, H. P. Lopuhaä and R. Kortlever, *Chem. Catal.*, 2024, **4**, 101065.
59 M. Gautam, F. Nkurunziza, B. Muchharla, B. Kumar and J. M. Spurgeon, *Anal. Chem.*, 2025, **97**, 5372–5392.
60 Q. Lei, L. Huang, J. Yin, B. Davaasuren, Y. Yuan, X. Dong, Z.-P. Wu, X. Wang, K. X. Yao, X. Lu and Y. Han, *Nat. Commun.*, 2022, **13**, 4857.
61 A. Dutta, M. Rahaman, B. Hecker, J. Drnec, K. Kiran, I. Zelocualtecatl Montiel, D. Jochen Weber, A. Zanetti, A. Cedeño López, I. Martens, P. Broekmann and M. Oezaslan, *J. Catal.*, 2020, **389**, 592–603.
62 H. Li, Y. Duan, Q. Feng, L. Wei, J. Zeng, Z. Chen, Q. Zhang, Y. Chen and Z. Yan, *Langmuir*, 2026, **42**, 12166–12175.
63 X. Cao, S. Ren, X. Zhang, Q. Fan, Q. Chen, J. Yang and J. Mao, *Chem*, 2024, **10**, 2089–2102.
64 L. Zhao, B. Xu, Z. Yuan, H. Dong, H. Zhao, D. Chen and X. Ding, *J. Environ. Chem. Eng.*, 2024, **12**, 111905.